A quantitative assessment of chemical perturbations in thermotropic cyanobiphenyls.

Sebastiano Guerra, Thibault Dutronc, Emmanuel Terazzi, Laure Guénée and Claude Piguet*

Supporting Information (39 pages)

Table S1 Elemental analyses for compounds **TBDPSO-$C_{10}H_{20}$-LC$^{i',j}$** , **TBDMSO-$C_{10}H_{20}$-LC$^{i',j}$**, and **HO-$C_{10}H_{20}$-LC$^{i',j}$**.

Compounds	Formula	*MM* g·mol^{-1}	%C found	%H found	%N found	%C calcd	%H calcd	%N calcd
TBDPSO-(0',0)	$C_{46}H_{51}NO_4Si \cdot 0.04CH_2Cl_2$	713.38	77.53	7.24	1.86	77.51	7.22	1.96
TBDPSO-(3',0)	$C_{47}H_{53}NO_4Si \cdot 0.2CH_2Cl_2$	741.00	76.49	7.48	1.70	76.51	7.26	1.89
TBDPSO-(2',0)	$C_{47}H_{53}NO_4Si \cdot 0.07CH_2Cl_2$	729.96	77.44	7.47	1.77	77.45	7.34	1.92
TBDPSO-(0',3)	$C_{47}H_{53}NO_4Si \cdot 0.05CH_2Cl_2$	728.26	77.57	7.43	1.77	77.60	7.35	1.92
TBDPSO-(2',0)	$C_{48}H_{55}NO_4Si \cdot 0.01CH_2Cl_2$	738.89	78.01	7.55	1.74	78.01	7.55	1.90
TBDMSO-(0',0)	$C_{36}H_{47}NO_4Si \cdot 0.01CH_2Cl_2$	586.70	73.74	8.19	2.28	73.74	8.19	2.39
TBDMSO-(3',0)	$C_{37}H_{49}NO_4Si$	599.87	73.96	8.38	2.20	74.08	8.23	2.33
TBDMSO-(2',0)	$C_{37}H_{49}NO_4Si \cdot 0.03CH_2Cl_2$	602.42	73.88	8.34	2.20	73.83	8.21	2.33
TBDMSO-(0',3)	$C_{37}H_{49}NO_4Si \cdot 0.04CH_2Cl_2$	603.27	73.79	8.35	2.19	73.74	8.20	2.32
TBDMSO-(2',0)	$C_{38}H_{51}NO_4Si \cdot 0.02CH_2Cl_2$	615.60	74.17	8.50	2.10	74.18	8.36	2.28
HO-(0',0)	$C_{30}H_{33}NO_4 \cdot 0.17H_2O$	474.47	75.93	7.15	2.74	75.92	7.08	2.95
HO-(3',0)	$C_{31}H_{35}NO_4 \cdot 0.90H_2O$	501.83	74.20	7.24	2.64	74.20	7.39	2.79
HO-(2',0)	$C_{31}H_{35}NO_4 \cdot 0.27H_2O$	490.48	75.92	7.32	2.69	75.91	7.30	2.86
HO-(0',3)	$C_{31}H_{35}NO_4 \cdot 0.50H_2O$	494.63	75.28	7.27	2.66	75.28	7.27	2.83
HO-(2',0)	$C_{32}H_{37}NO_4 \cdot 0.28H_2O$	504.68	76.15	7.54	2.59	76.14	7.54	2.77

Table S2 Thermogravimetric analysis for the decomposition of **TBDPSO-$C_{10}H_{20}$-LC$^{i',j}$**, **TBDMSO-$C_{10}H_{20}$-LC$^{i',j}$**, and **HO-$C_{10}H_{20}$-LC$^{i',j}$**.

Compounds	*T* /°C (K)	Weight loss /%
HO-$C_{10}H_{20}$-LC$^{0',0}$	220 (493)	40.8
	315 (588)	56.1
HO-$C_{10}H_{20}$-LC$^{3',0}$	215 (488)	35.5
	320 (593)	58.3
HO-$C_{10}H_{20}$-LC$^{2',0}$	200 (473)	41.1
	310 (583)	54.3
HO-$C_{10}H_{20}$-LC$^{0',3}$	200 (473)	42.6
	315 (588)	48.3
HO-$C_{10}H_{20}$-LC$^{2',2}$	190 (463)	45.8
	315 (588)	47.1
TBDMSO-$C_{10}H_{20}$-LC$^{0',0}$	270 (543)	99.6
TBDMSO-$C_{10}H_{20}$-LC$^{3',0}$	270 (543)	99.0
TBDMSO-$C_{10}H_{20}$-LC$^{2',0}$	280 (553)	99.1
TBDMSO-$C_{10}H_{20}$-LC$^{0',3}$	235 (508)	93.1
TBDMSO-$C_{10}H_{20}$-LC$^{2',2}$	240 (513)	96.7
TBDPSO-$C_{10}H_{20}$-LC$^{0',0}$	270 (543)	95.8
TBDPSO-$C_{10}H_{20}$-LC$^{3',0}$	280 (553)	97.8
TBDPSO-$C_{10}H_{20}$-LC$^{2',0}$	280 (553)	90.2
TBDPSO-$C_{10}H_{20}$-LC$^{0',3}$	240 (513)	89.9
TBDPSO-$C_{10}H_{20}$-LC$^{2',2}$	290 (563)	94.5

Table S3 Small-angle X-ray scaterring data collected in the smectic A mesophases for **TBDMSO-$C_{10}H_{20}$-LC$^{i',j}$** and **TBDPSO-$C_{10}H_{20}$-LC$^{i',j}$**.

Compounds	T / K	State	2θ / deg	d_{hkl} / Å	$00l$	I / a.u. [a]
TBDMSO-$C_{10}H_{20}$-LC$^{0',0}$	393	SmA	1.79	49.21	001	Vs
			3.60	24.52	002	Vw
TBDMSO-$C_{10}H_{20}$-LC$^{3',0}$	373	SmA	1.79	49.32	001	s
TBDMSO-$C_{10}H_{20}$-LC$^{2',0}$	353	SmA	1.78	49.69	001	s
TBDMSO-$C_{10}H_{20}$-LC$^{0',3}$	373	SmA	1.94	45.64	001	s
			3.88	22.78	002	Vw (sh)
TBDMSO-$C_{10}H_{20}$-LC$^{2',2}$	263	SmA	1.73	51.20	001	s
TBDPSO-$C_{10}H_{20}$-LC$^{0',0}$	323	SmA	1.62	54.52	001	Vh
			3.25	27.17	002	Vw
TBDPSO-$C_{10}H_{20}$-LC$^{3',0}$	293	SmA	1.64	53.92	001	m
TBDPSO-$C_{10}H_{20}$-LC$^{2',0}$	273	SmA	1.58	56.03	001	m
			3.13	28.26	002	Vw (sh)
TBDPSO-$C_{10}H_{20}$-LC$^{0',3}$	293	SmA	1.72	51.32	001	m
			3.47	25.48	002	w

[a] w = weak, m = medium, s = strong, V = very, sh = shoulder.

Table S4 Thermodynamic parameters (ΔH_{tr} and ΔS_{tr}) and transition temperatures (T_{tr}) for the phase transitions **$H_{25}C_{12}$-LC$^{i',j}$**,[16] **HO-$C_{10}H_{20}$-LC$^{i',j}$**, **TBDMSO-$C_{10}H_{20}$-LC$^{i',j}$** and **TBDPSO-$C_{10}H_{20}$-LC$^{i',j}$** and associated cohesive free energies in the solid ($CFED_{solid}$) and liquid crystalline ($CFED_{liq\text{-}cryst}$) states (Scan rate = 0.5 K·min^{-1}).

Compounds	V_{mol} [a] /mol·cm^{-3}	$\Delta H_{melting}$ [b] /kJ·mol^{-1}	$\Delta S_{melting}$ [b] /J·mol^{-1}·K^{-1}	$T_{melting}$ /K	$CFED_{solid}$ [c] /J·cm^{-3}	$\Delta H_{clearing}$ [b] /kJ·mol^{-1}	$\Delta S_{clearing}$ [b] /J·mol^{-1}·K^{-1}	$T_{clearing}$ /K	$CFED_{liq\text{-}cryst}$ [d] /J·cm^{-3}
$H_{25}C_{12}$-LC$^{0',0}$	488.5	46.0(5)	123(1)	373	3.2(7)	3.66(7)	7.5(1)	491	1.5(2)
$H_{25}C_{12}$-LC$^{3',0}$	504.1	38.3(4)	104(1)	368	1.6(5)	1.57(3)	3.7(1)	426	0.24(8)
$H_{25}C_{12}$-LC$^{2',0}$	503.4	43.7(4)	123(2)	354	-1.5(6)	1.19(2)	2.9(1)	406	0.07(7)
$H_{25}C_{12}$-LC$^{0',3}$	503.5	52.8(5)	147(2)	359	-0.4(7)	0.70(2)	1.7(1)	422	0.10(4)
$H_{25}C_{12}$-LC$^{2',2}$	517.7	53.9(5)	148(2)	364	1.1(7)	[f]	[f]	[f]	[f]
HO-$C_{10}H_{20}$-LC$^{0',0}$	472.0	28.7(3)	73.8(7)	389	4.8(4)	1.12((2)	2.3(1)	484	0.41(6)
HO-$C_{10}H_{20}$-LC$^{3',0}$	489.2	[e]	[e]	[e]	[e]	0.70(1)	1.6(1)	434	0.11(4)
HO-$C_{10}H_{20}$-LC$^{2',0}$	489.0	27.2(3)	74.2(7)	377	1.3(4)	1.20(2)	3.0(1)	408	0.00(7)
HO-$C_{10}H_{20}$-LC$^{0',3}$	488.7	26.1(3)	69.5(7)	376	2.5(4)	0.51(1)	1.20(1)	409	0.05(3)
HO-$C_{10}H_{20}$-LC$^{2',2}$	503.6	42.4(4)	112(1)	378	4.4(6)	[f]	[f]	[f]	[f]
TBDMSO-$C_{10}H_{20}$-LC$^{0',0}$	604.0	19.5(2)	58.2(6)	335	-2.3(2)	6.1(1)	13.4(3)	458	1.2(3)
TBDMSO-$C_{10}H_{20}$-LC$^{3',0}$	622.6	[e]	[e]	[e]	[e]	3.28(7)	8.4(2)	390	-0.1(2)

TBDMSO-$C_{10}H_{20}$-LC$^{2',0}$	622.1	17.7(2)	55.0(6)	321	-3.3(2)	3.19(6)	8.8(2)	363	-0.5(2)
TBDMSO-$C_{10}H_{20}$-LC$^{0',3}$	622.2	20.9(2)	62.3(6)	336	-2.3(2)	4.09(8)	10.2(2)	402	-0.0(2)
TBDMSO-$C_{10}H_{20}$-LC$^{2',2}$	637.4	32.3(3)	98(1)	328	-4.7(4)	*f*	*f*	*f*	*f*
TBDPSO-$C_{10}H_{20}$-LC$^{0',0}$	716.1	*e*	*e*	*e*	*e*	11.9(2)	30.3(6)	391	-0.4(5)
TBDPSO-$C_{10}H_{20}$-LC$^{3',0}$	730.5	*e*	*e*	*e*	*e*	1.50(3)	4.7(1)	319	-0.53(7)
TBDPSO-$C_{10}H_{20}$-LC$^{2',0}$	729.0	*e*	*e*	*e*	*e*	0.420(8)	1.50(1)	285	-0.24(2)
TBDPSO-$C_{10}H_{20}$-LC$^{0',3}$	729.7	*e*	*e*	*e*	*e*	0.57(1)	1.70(1)	332	-0.18(2)
TBDPSO-$C_{10}H_{20}$-LC$^{2',2}$	744.5	*e*	*e*	*e*	*e*	*f*	*f*	*f*	*f*

[a] The specific molar volumes V_{mol} are deduced from the Connolly volume estimated for the optimized gas-phase structures $V_{mol} = N_{Av} \cdot V_{molecule}$.[28] [b] Obtained by DSC at the transition temperatures (0.5 K/min). [c] $CFED_{solid} = \Delta G^{T^{ref}}_{cohesion,m} / V_{mol} = \Delta H^{T^{ref}}_{m} - T^{ref} \Delta S^{T^{ref}}_{m}$ with T^{ref}_{m} = 358.3 K (eq. 6). [d] $CFED_{liq\text{-}cryst} = \Delta G^{T^{ref}}_{cohesion,c} / V_{mol} = \Delta H^{T^{ref}}_{c} - T^{ref} \Delta S^{T^{ref}}_{c}$ with $T^{ref}_{clearing}$ = 401.3 K (eq. 7). [e] Glass transition. [f] Non-mesogenic.

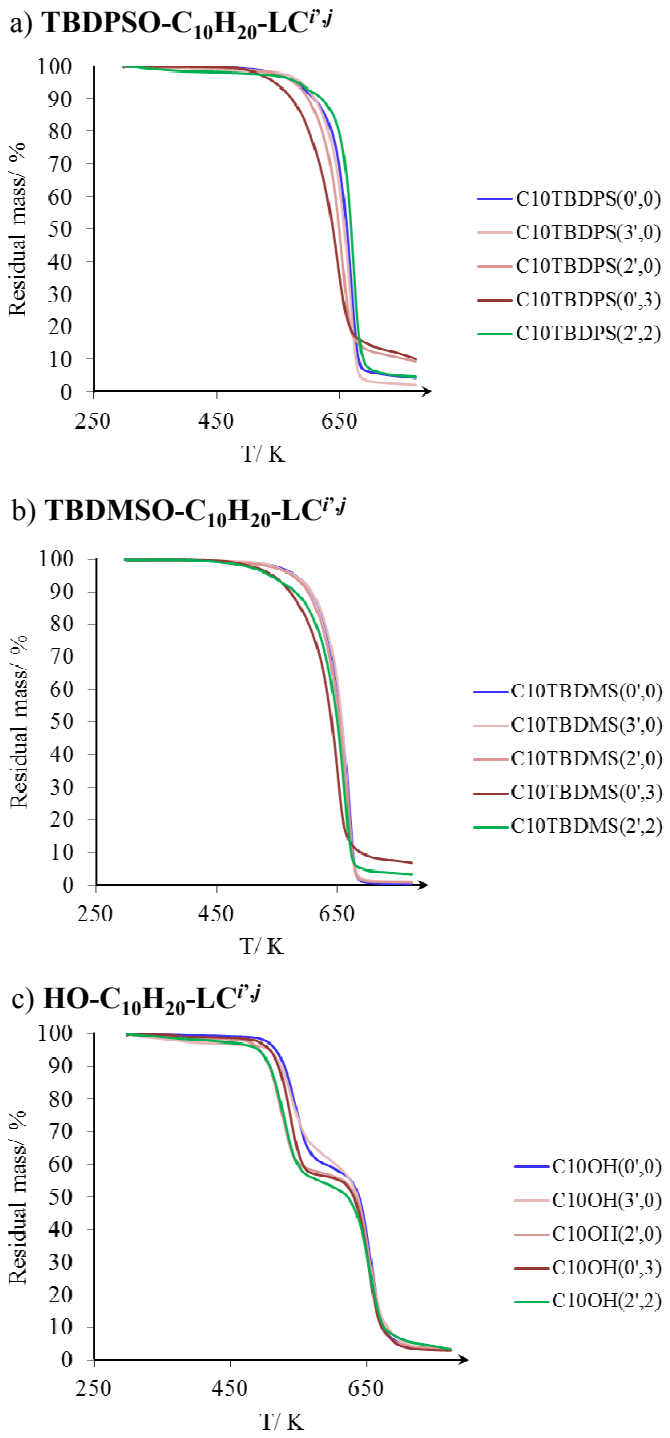

Figure S1 Thermogravimetric traces recorded at 10 K·min^{-1} for a) **TBDPSO-$C_{10}H_{20}$-LC$^{i',j}$**, b) **TBDMSO-$C_{10}H_{20}$-LC$^{i',j}$** and c) **HO-$C_{10}H_{20}$-LC$^{i',j}$**

HO-$C_{10}H_{20}$-LC$^{3',0}$, 418 K

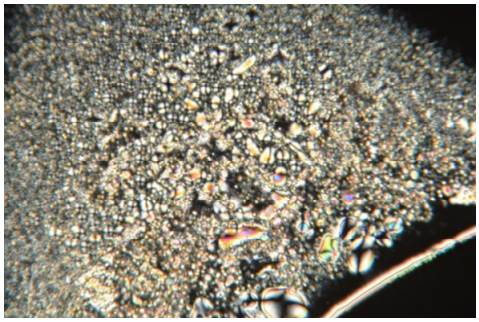

Schlieren textures
Nematic

HO-$C_{10}H_{20}$-LC$^{2',0}$, 411 K

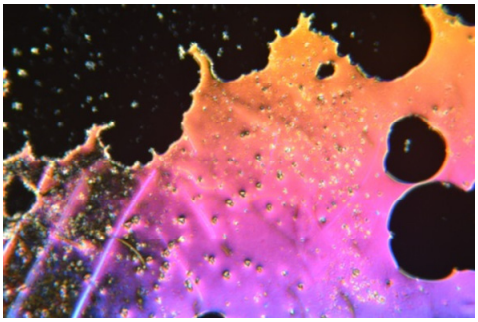

Not textured, highly colored
Nematic

HO-$C_{10}H_{20}$-LC$^{0',3}$, 410 K

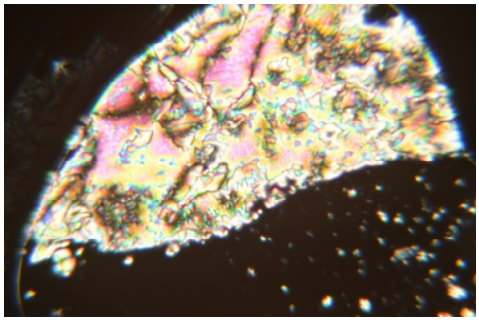

Schlieren textures
Nematic

HO-$C_{10}H_{20}$-LC$^{2',2}$, 303 K

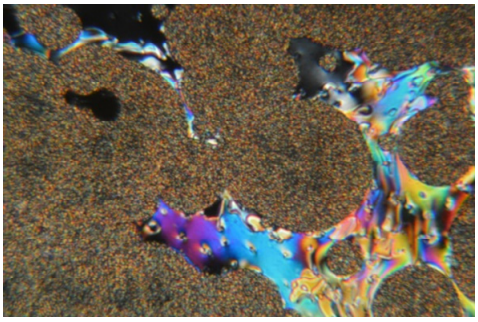

Schlieren textures
Monotropic nematic

Figure S2 Polarized optical micrographs of **HO-$C_{10}H_{20}$-LC$^{i',j}$** compounds in their liquid crystalline states.

TBDMSO-$C_{10}H_{20}$-LC$^{0',0}$, 432 K

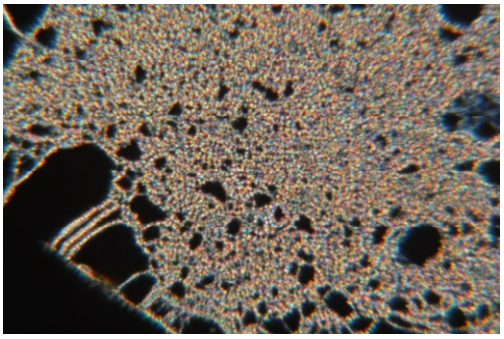

Unresolved focal conic fan textures
Smectic A

TBDMSO-$C_{10}H_{20}$-LC$^{3',0}$, 313 K

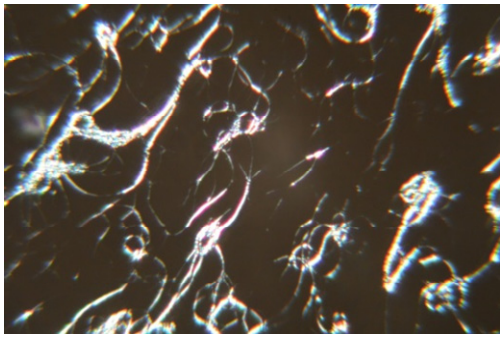

Bangle-like textures of the homeotropic areas
Smectic A

TBDMSO-$C_{10}H_{20}$-LC$^{2',0}$, 363 K

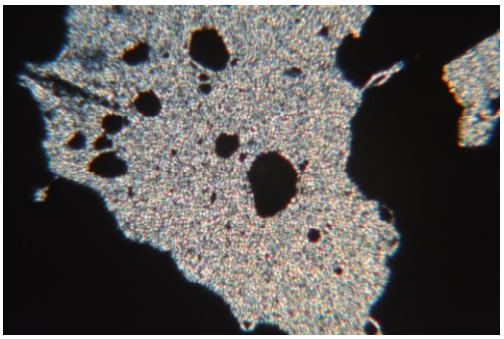

Focal conic fan textures with homeotropic areas
Smectic A

TBDMSO-$C_{10}H_{20}$-LC$^{0',3}$, 373 K

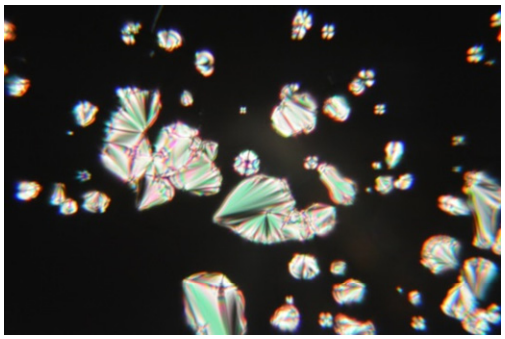

Focal conic fan textures with homeotropic areas
Smectic A

Figure S3 Polarized optical micrographs of **TPDMSO-$C_{10}H_{20}$-LC$^{i',j}$** compounds in their liquid crystalline states. The clearing temperature at 283 K for **TPDMSO-$C_{10}H_{20}$-LC$^{2',2}$** is below the temperature range accessible for our POM setup.

TBDPSO-$C_{10}H_{20}$-LC$^{0',0}$, 355 K

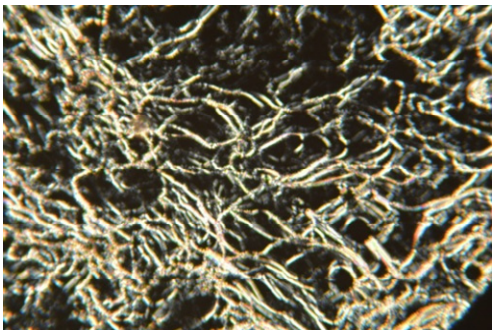

Bangle-like textures of the homeotropic areas
Smectic A

TBDPMSO-$C_{10}H_{20}$-LC$^{3',0}$, 315 K

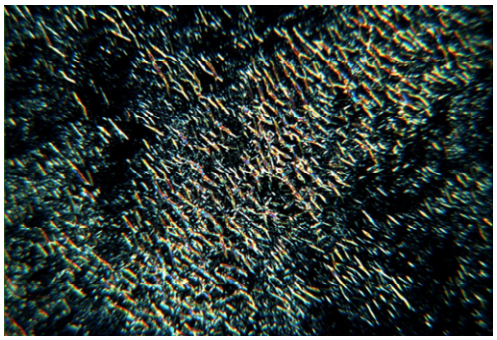

Bangle-like textures of the homeotropic areas
Smectic A

TBDPSO-$C_{10}H_{20}$-LC$^{2',0}$, 304 K

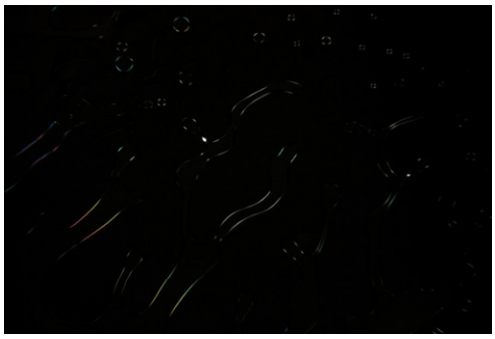

Weak birefringence in homeotropic areas
Smectic A

TBDPSO-$C_{10}H_{20}$-LC$^{0',3}$, 308 K

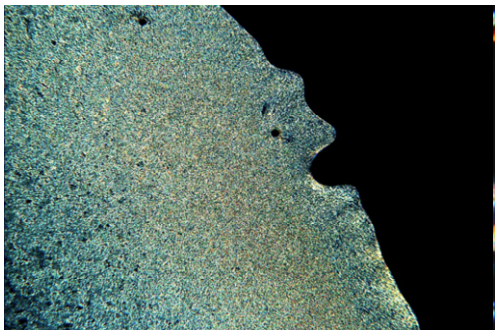

Unresolved focal conic fan textures
Smectic A

Figure S4 Polarized optical micrographs of **TPDPSO-$C_{10}H_{20}$-LC$^{i',j}$** compounds in their liquid crystalline states.

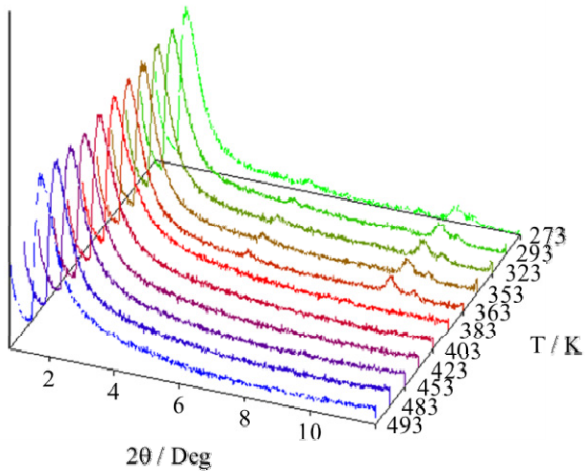

Figure S5 VT-small-angle X-ray diffractograms recorded for **HO-C$_{10}$H$_{20}$-LC$^{0',0}$**.

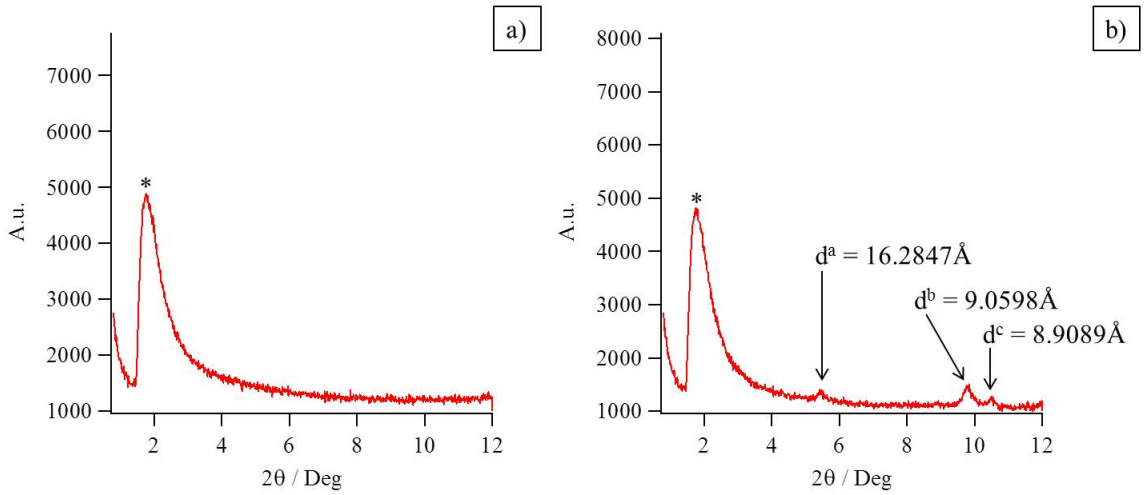

Figure S6 Diffractograms of **HO-C$_{10}$H$_{20}$-LC$^{0',0}$** within a) the nematic phase (N) at T = 423K, and b) the crystalline state (Cr) at T = 363K. * corresponds to capillary noise.

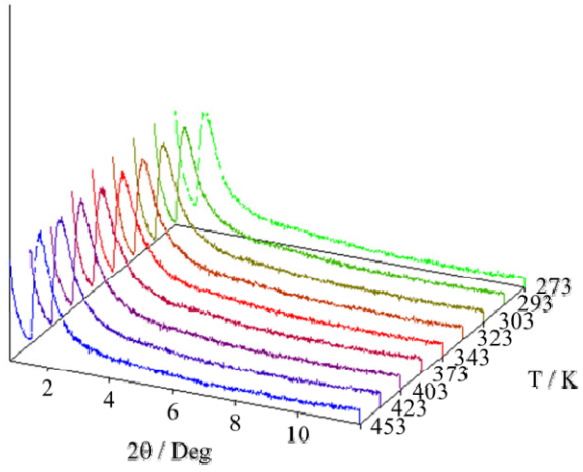

Figure S7 VT-small-angle X-ray diffractograms recorded for **HO-C$_{10}$H$_{20}$-LC$^{3',0}$**.

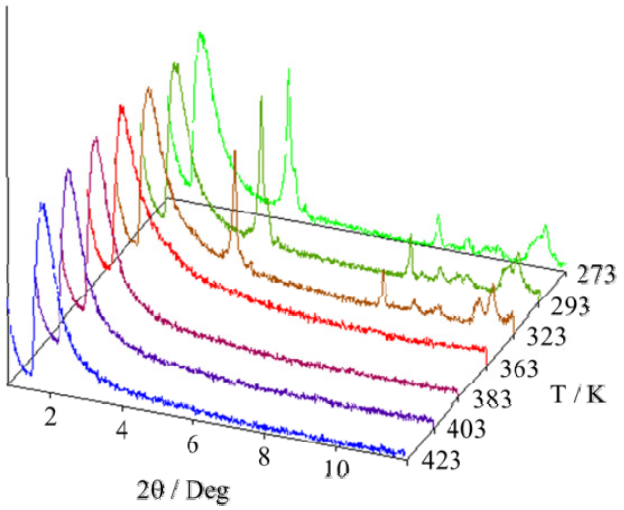

Figure S8 VT-small-angle X-ray diffractograms recorded for **HO-C$_{10}$H$_{20}$-LC$^{2',0}$**.

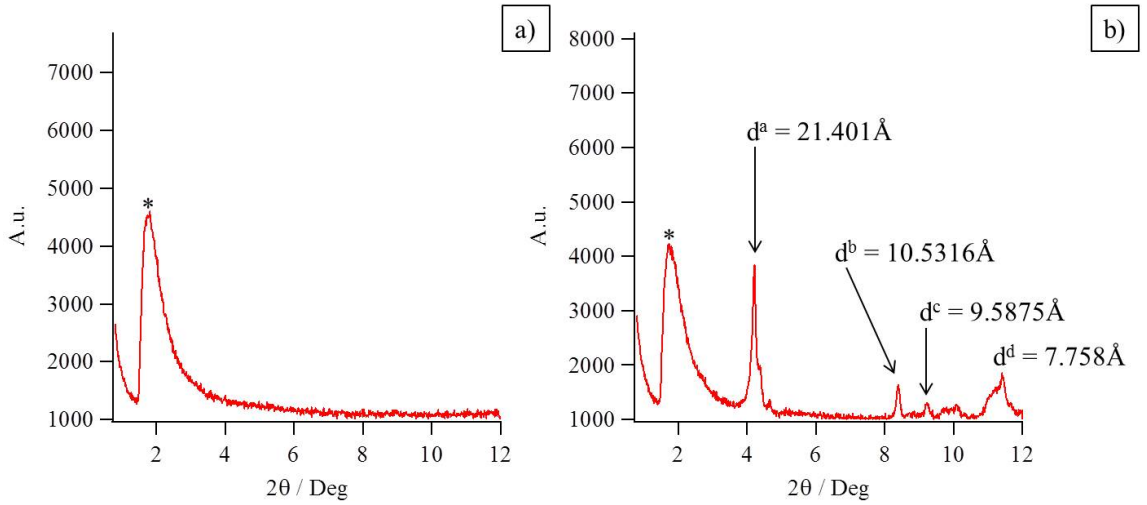

Figure S9 Diffractograms of **HO-C$_{10}$H$_{20}$-LC$^{2',0}$** within a) the nematic phase (N) at T = 383K, and b) the crystalline state (Cr) at T = 273K. * corresponds to capillary noise.

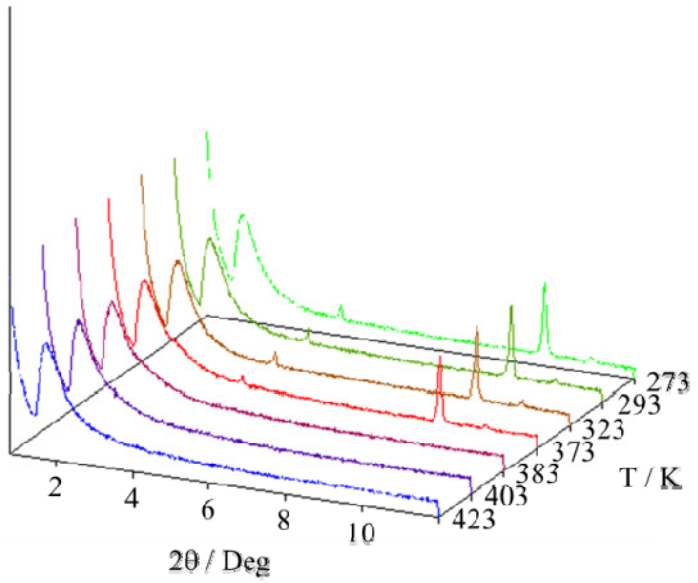

Figure S10 VT-small-angle X-ray diffractograms recorded for **HO-C$_{10}$H$_{20}$-LC$^{0',3}$**.

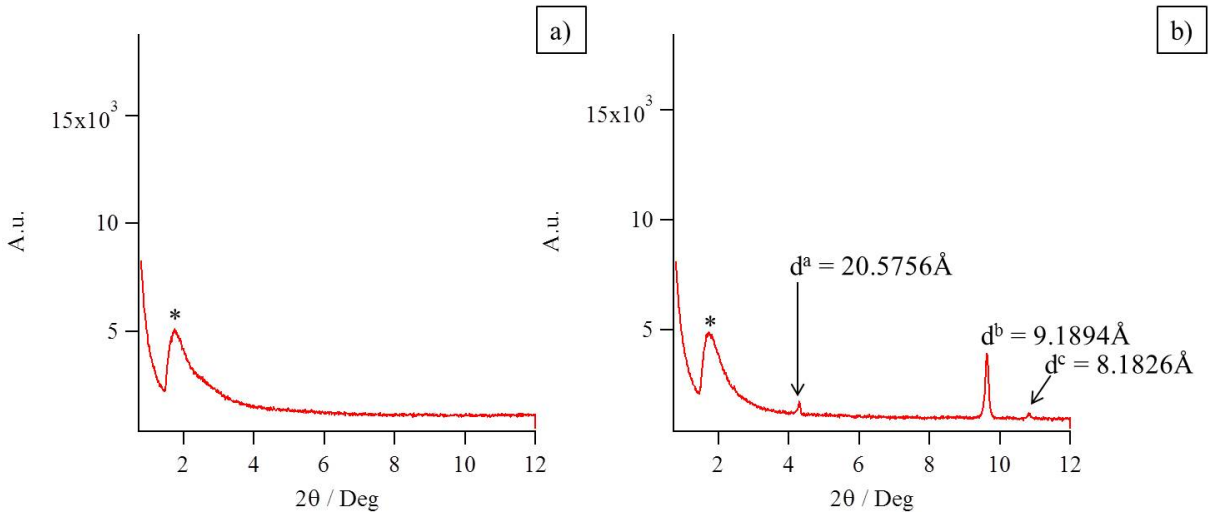

Figure S11 Diffractograms of **HO-C$_{10}$H$_{20}$-LC$^{0',3}$** within a) the nematic phase (N) at T = 383K, and b) the crystalline state (Cr) at T = 273K. * correspond to capillary noise.

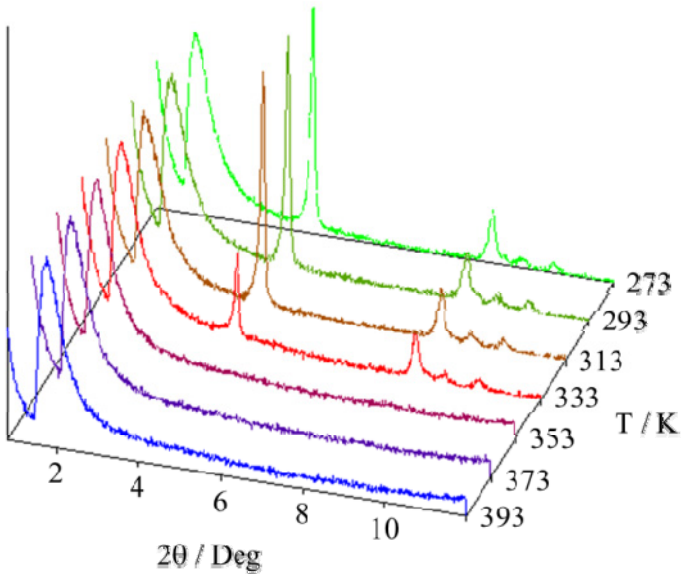

Figure S12 VT-small-angle X-ray diffractograms recorded for **HO-C$_{10}$H$_{20}$-LC$^{2',2}$**.

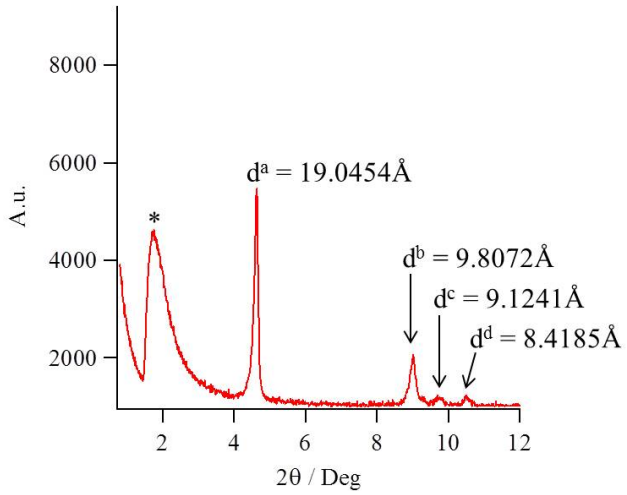

Figure S13 Diffractograms of **HO-C$_{10}$H$_{20}$-LC$^{2',2}$** within the crystalline state (Cr) at T = 273K. * corresponds to capillary noise.

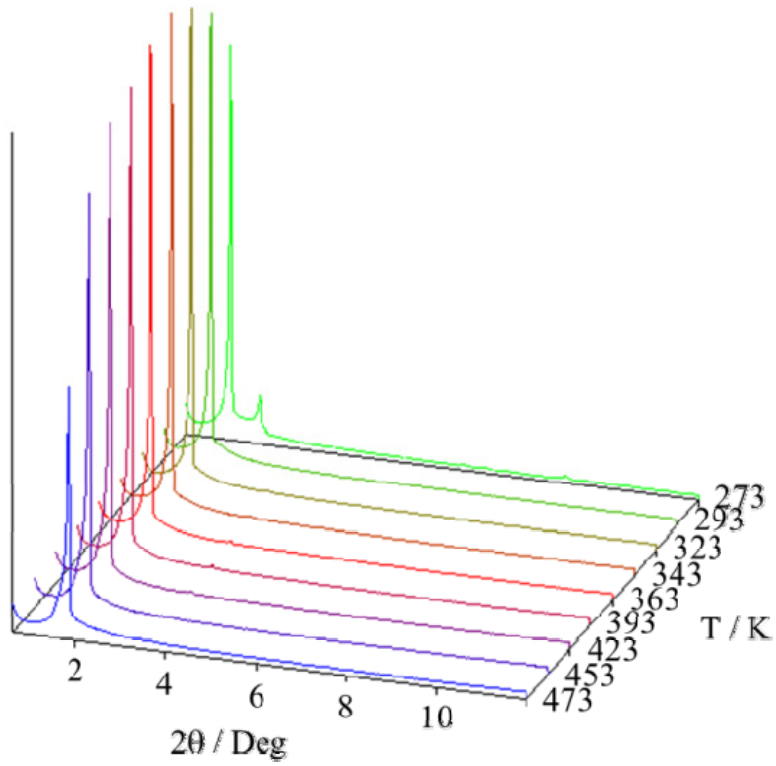

Figure S14 VT-small-angle X-ray diffractograms recorded for **TBDMSO-$C_{10}H_{20}$-LC$^{0',0}$**.

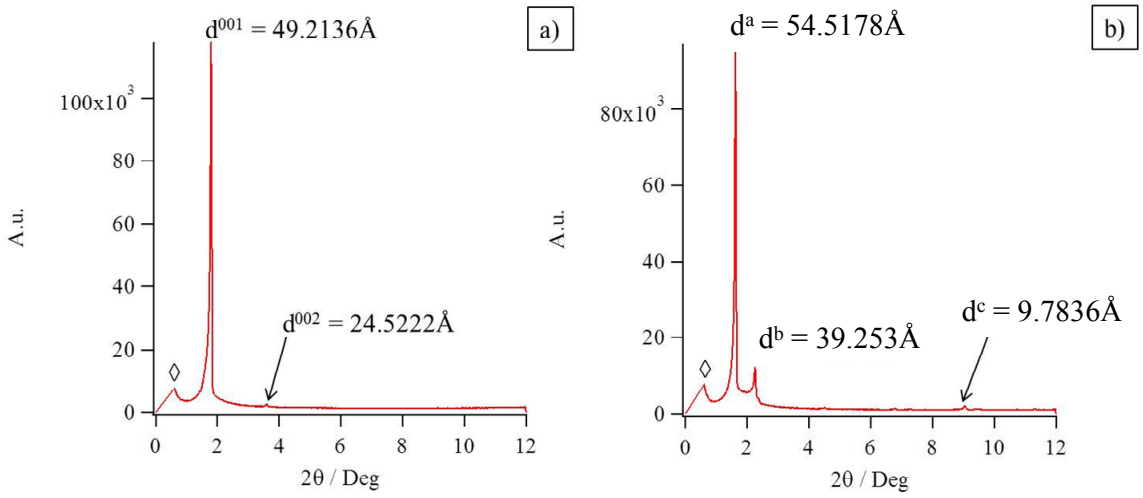

Figure S15 Diffractograms of **TBDMSO-$C_{10}H_{20}$-LC$^{0',0}$** within a) the smectic A phase (SmA) at T = 393K, and b) the crystalline state (Cr) at T = 273K. ◊ corresponds to primary beam residue.

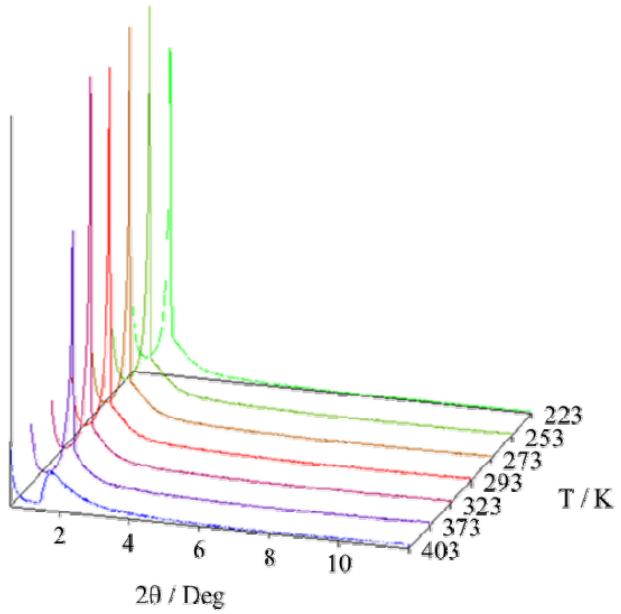

Figure S16 VT-small-angle X-ray diffractograms recorded for **TBDMSO-$C_{10}H_{20}$-LC$^{3',0}$**.

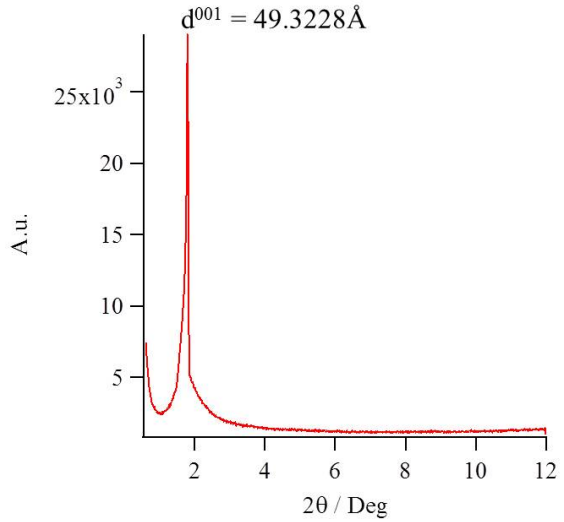

Figure S17 Diffractograms of **TBDMSO-$C_{10}H_{20}$-LC$^{3',0}$** within the smectic A phase (SmA) at T = 373K.

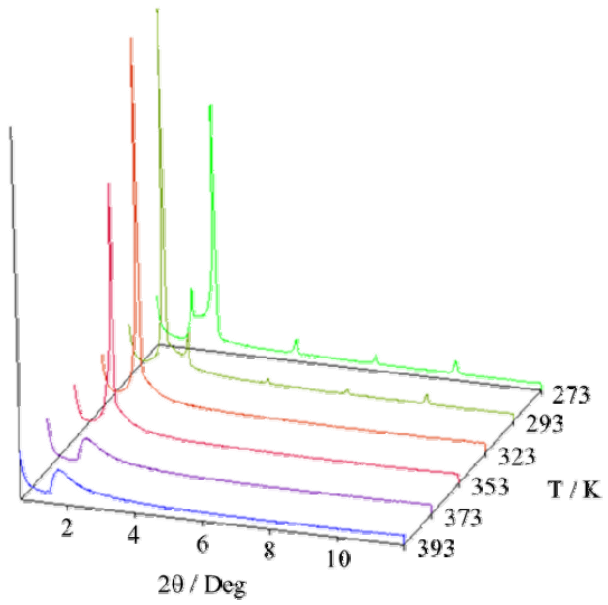

Figure S18 VT-small-angle X-ray diffractograms recorded for **TBDMSO-$C_{10}H_{20}$-LC$^{2',0}$**.

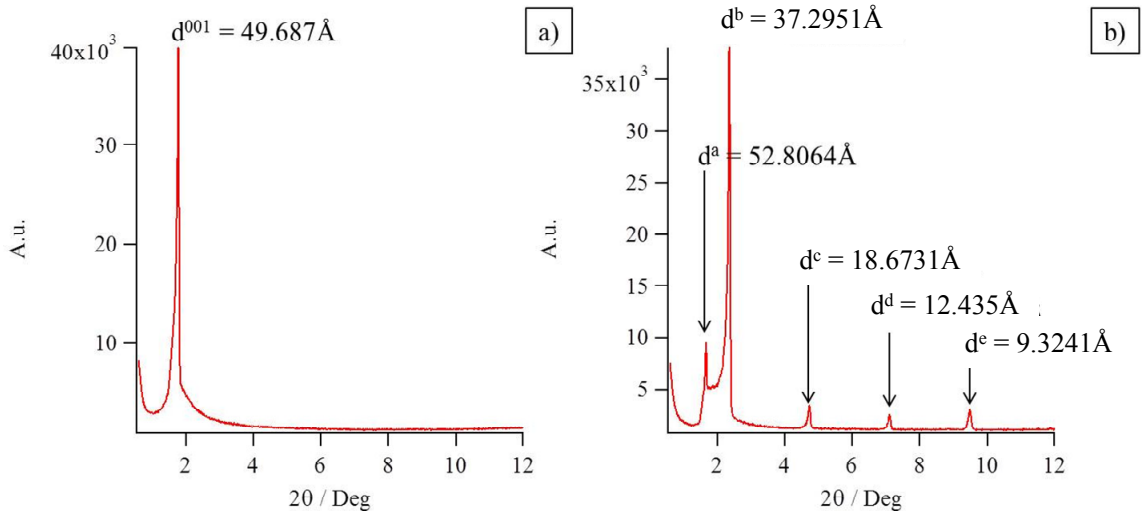

Figure S19 Diffractograms of **TBDMSO-$C_{10}H_{20}$-LC$^{2',0}$** within a) the smectic A phase (SmA) at T = 353K, and b) the crystalline state (Cr) at T = 273K.

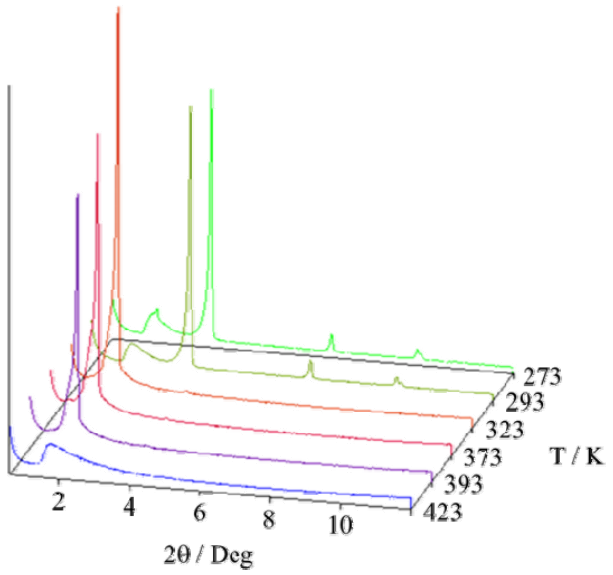

Figure S20 VT-small-angle X-ray diffractograms recorded for **TBDMSO-$C_{10}H_{20}$-LC$^{0',3}$**.

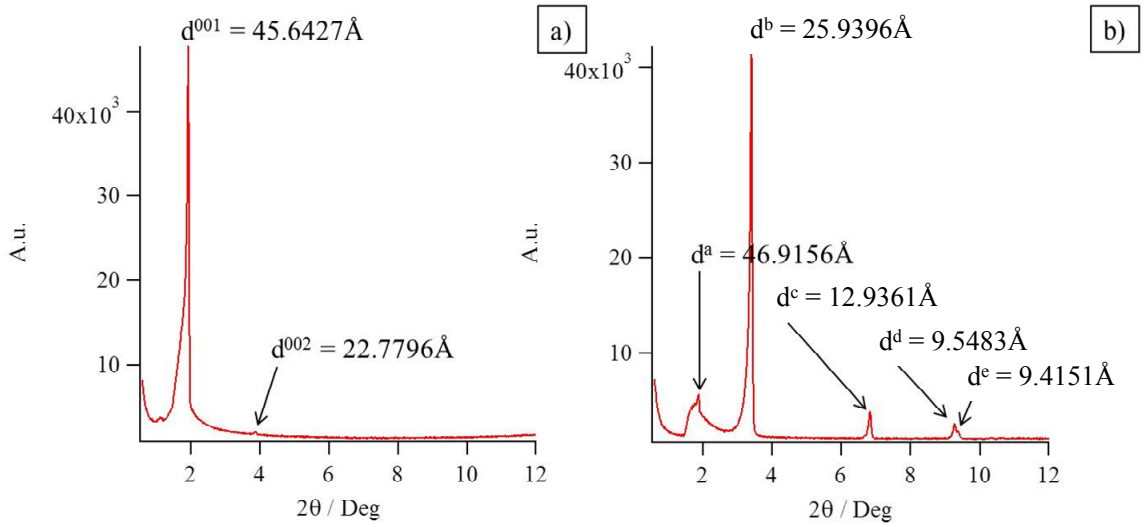

Figure S21 Diffractograms of **TBDMSO-$C_{10}H_{20}$-LC$^{0',3}$** within a) the smectic A phase (SmA) at T = 373K, and b) the crystalline state (Cr) at T = 273K.

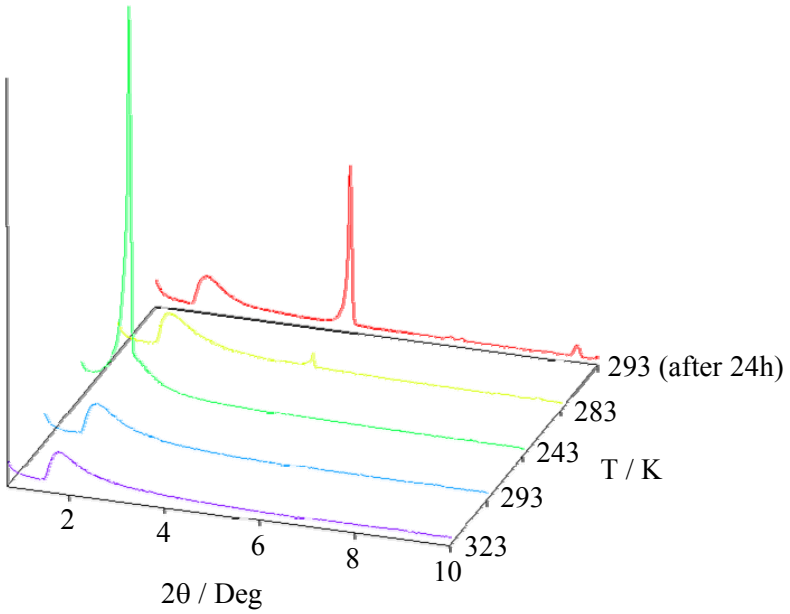

Figure S22 VT-small-angle X-ray diffractograms recorded for **TBDMSO-$C_{10}H_{20}$-LC$^{2',2}$**.

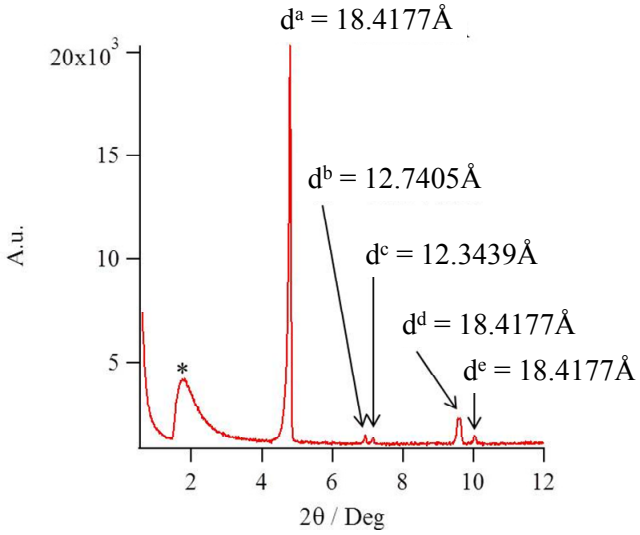

Figure S23 Diffractograms of **TBDMSO-$C_{10}H_{20}$-LC$^{2',2}$** within the crystalline state at T =273K. * corresponds to capillary noise.

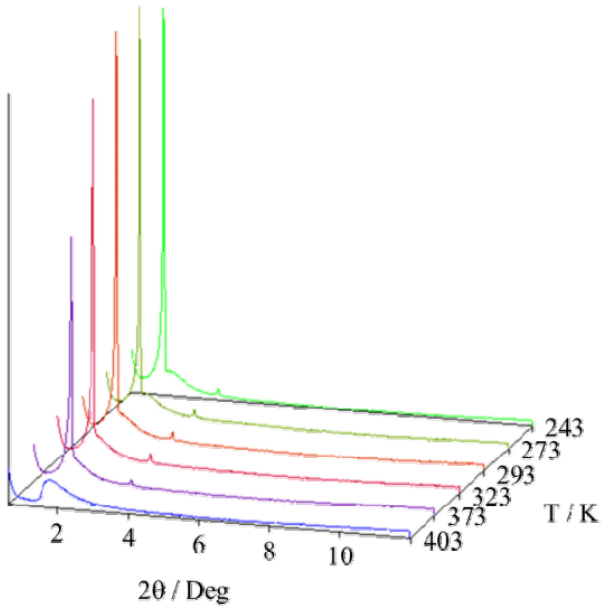

Figure S24 VT-small-angle X-ray diffractograms recorded for **TBDPSO-$C_{10}H_{20}$-LC$^{0',0}$**.

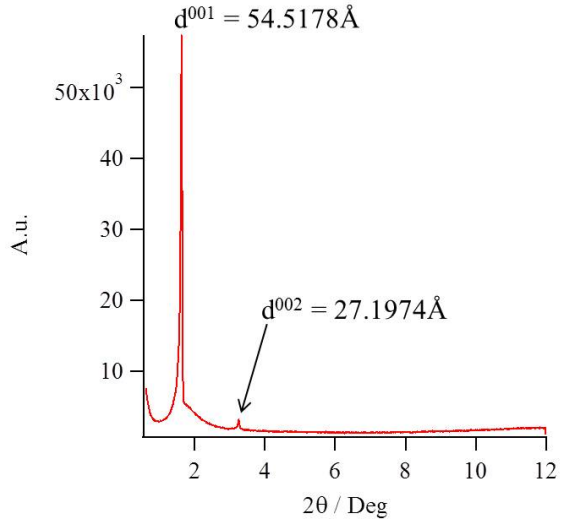

Figure S25 Diffractograms of **TBDPSO-$C_{10}H_{20}$-LC$^{0',0}$** within the smectic A phase (SmA) at T = 323K.

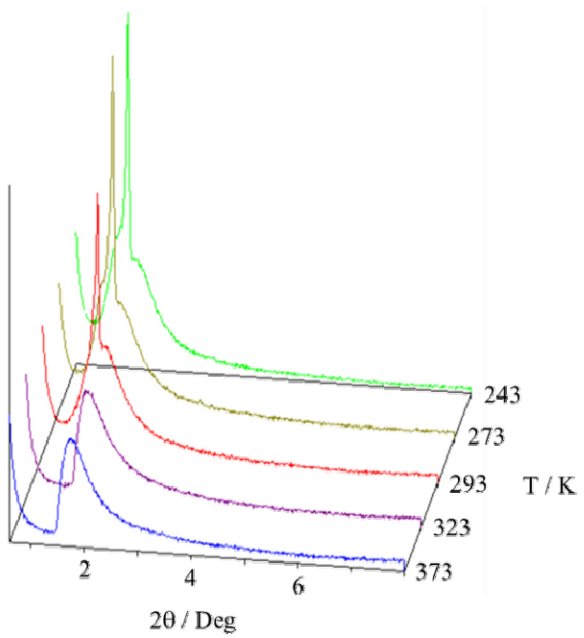

Figure S26 VT-small-angle X-ray diffractograms recorded for **TBDPSO-$C_{10}H_{20}$-LC$^{3',0}$**.

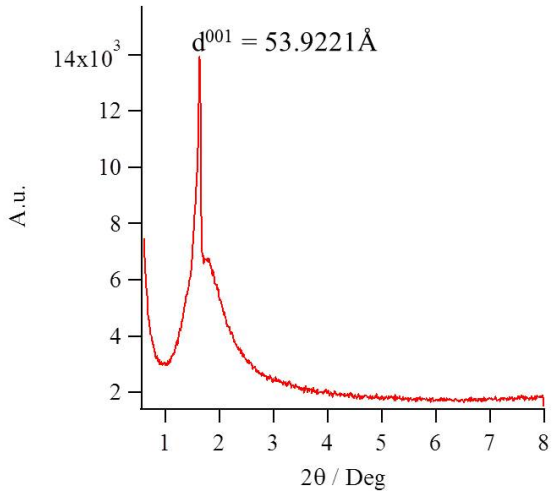

Figure S27 Diffractograms of **TBDPSO-$C_{10}H_{20}$-LC$^{3',0}$** within the smectic A phase (SmA) at T =293K.

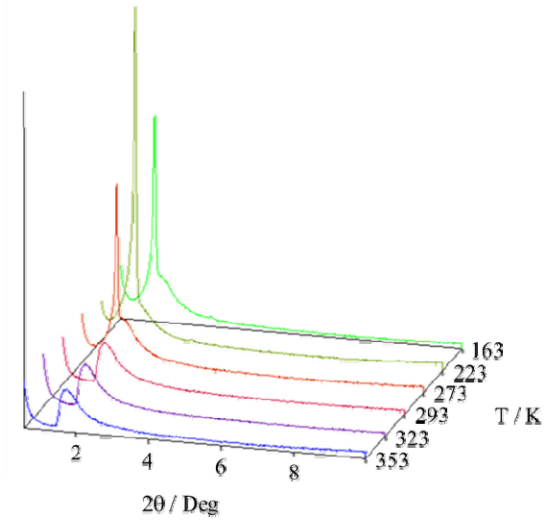

Figure S28 VT-small-angle X-ray diffractograms recorded for **TBDPSO-$C_{10}H_{20}$-LC$^{2',0}$**.

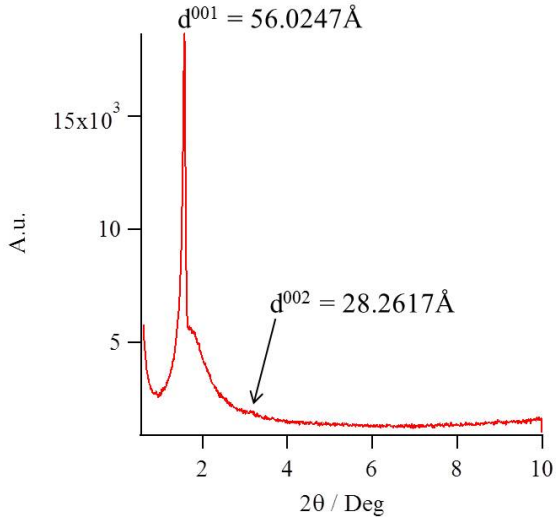

Figure S29 Diffractograms of **TBDPSO-$C_{10}H_{20}$-LC$^{2',0}$** within the smectic A phase (SmA) at T = 273K.

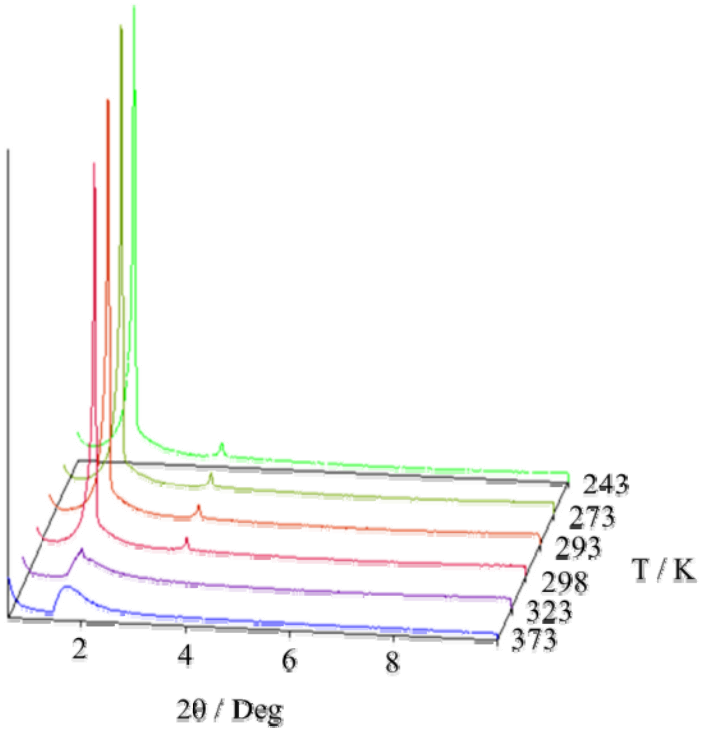

Figure S30 VT-small-angle X-ray diffractograms recorded for **TBDPSO-$C_{10}H_{20}$-LC$^{0',3}$**.

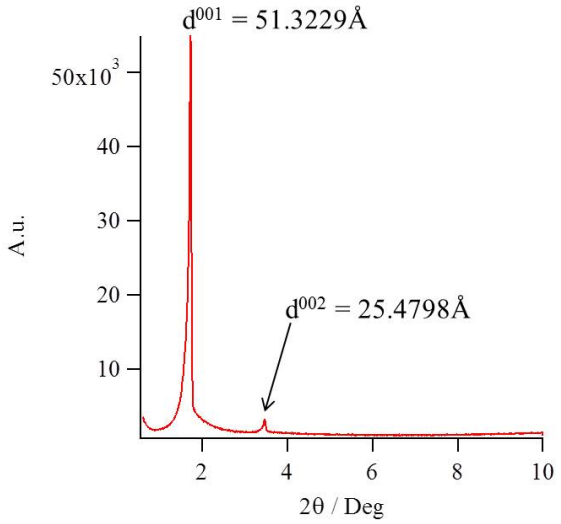

Figure S31 Diffractograms of **TBDPSO-$C_{10}H_{20}$-LC$^{0',3}$** within the smectic A phase (SmA) at T = 293K.

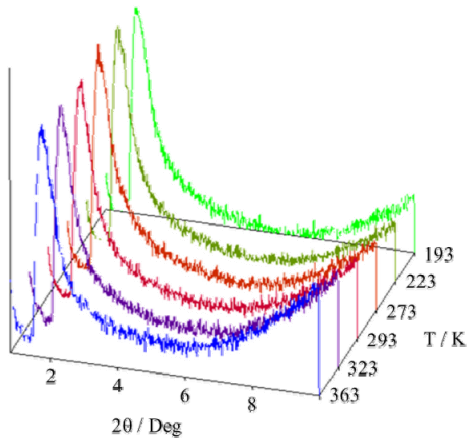

Figure S32 VT-small-angle X-ray diffractograms recorded for **TBDPSO-C$_{10}$H$_{20}$-LC$^{2',2}$**

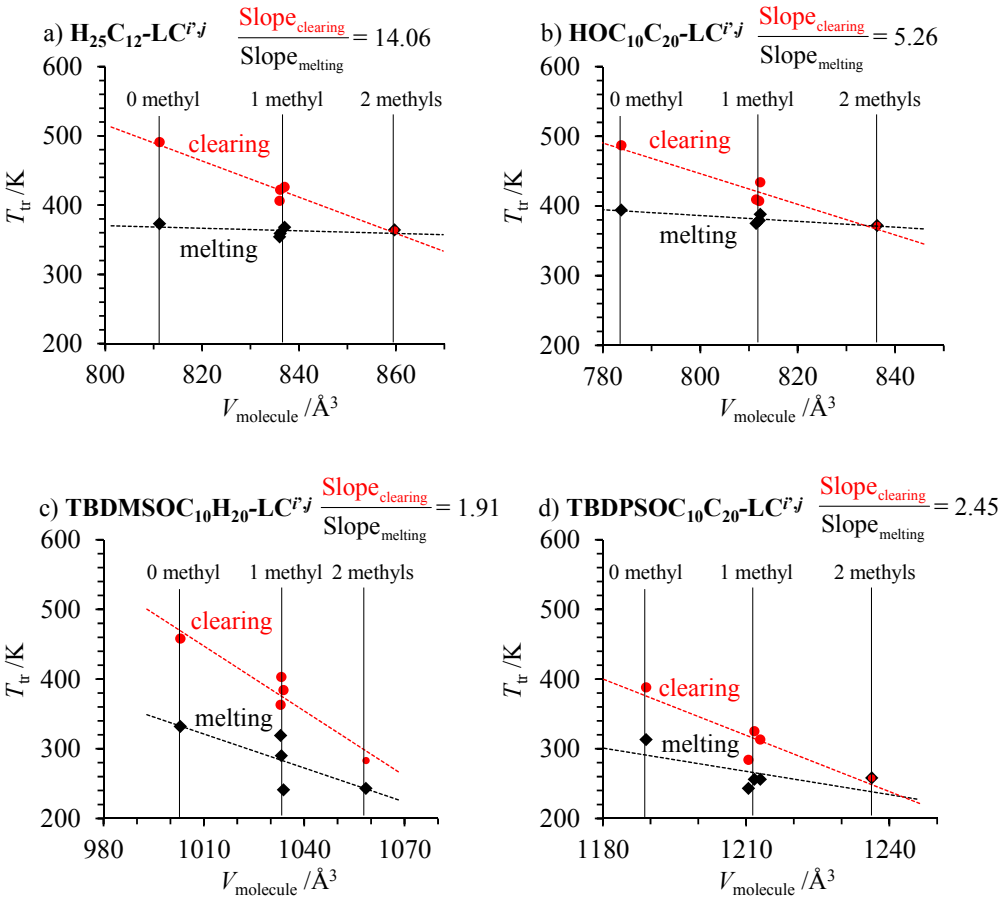

Figure S33 Melting and clearing temperatures observed in **H$_{25}$C$_{12}$-LC$^{i',j}$**,[16] **HO-C$_{10}$H$_{20}$-LC$^{i',j}$**, **TBDMSO-C$_{10}$H$_{20}$-LC$^{i',j}$** and **TBDPSO-C$_{10}$H$_{20}$-LC$^{i',j}$** upon successive methylation of the aromatic cyanobiphenyl cores. $V_{molecule}$ are the Connolly volumes[28] computed for the gas-phase optimized structures (see Table A1-1). The linear dotted lines are guides for the eyes

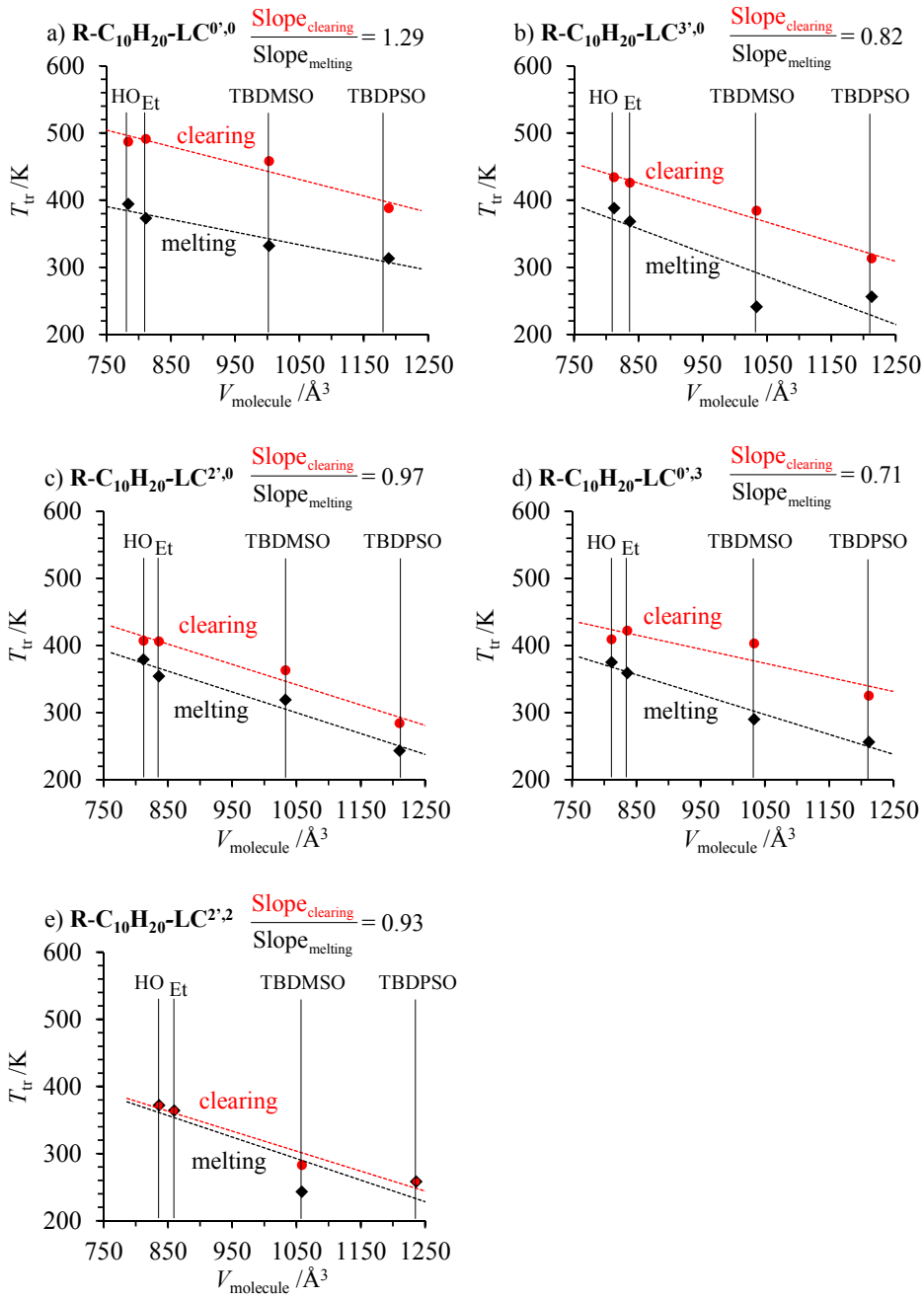

Figure S34 Melting and clearing temperatures observed in **$H_{25}C_{12}$-LC$^{i',j}$**,[16] **HO-$C_{10}H_{20}$-LC$^{i',j}$**, **TBDMSO-$C_{10}H_{20}$-LC$^{i',j}$** and **TBDPSO-$C_{10}H_{20}$-LC$^{i',j}$** upon successive substitution of the flexible alkyl chains. $V_{molecule}$ are the Connolly volumes[28] computed for the gas-phase optimized structures (see Table A1-1). The linear dotted lines are guides for the eyes

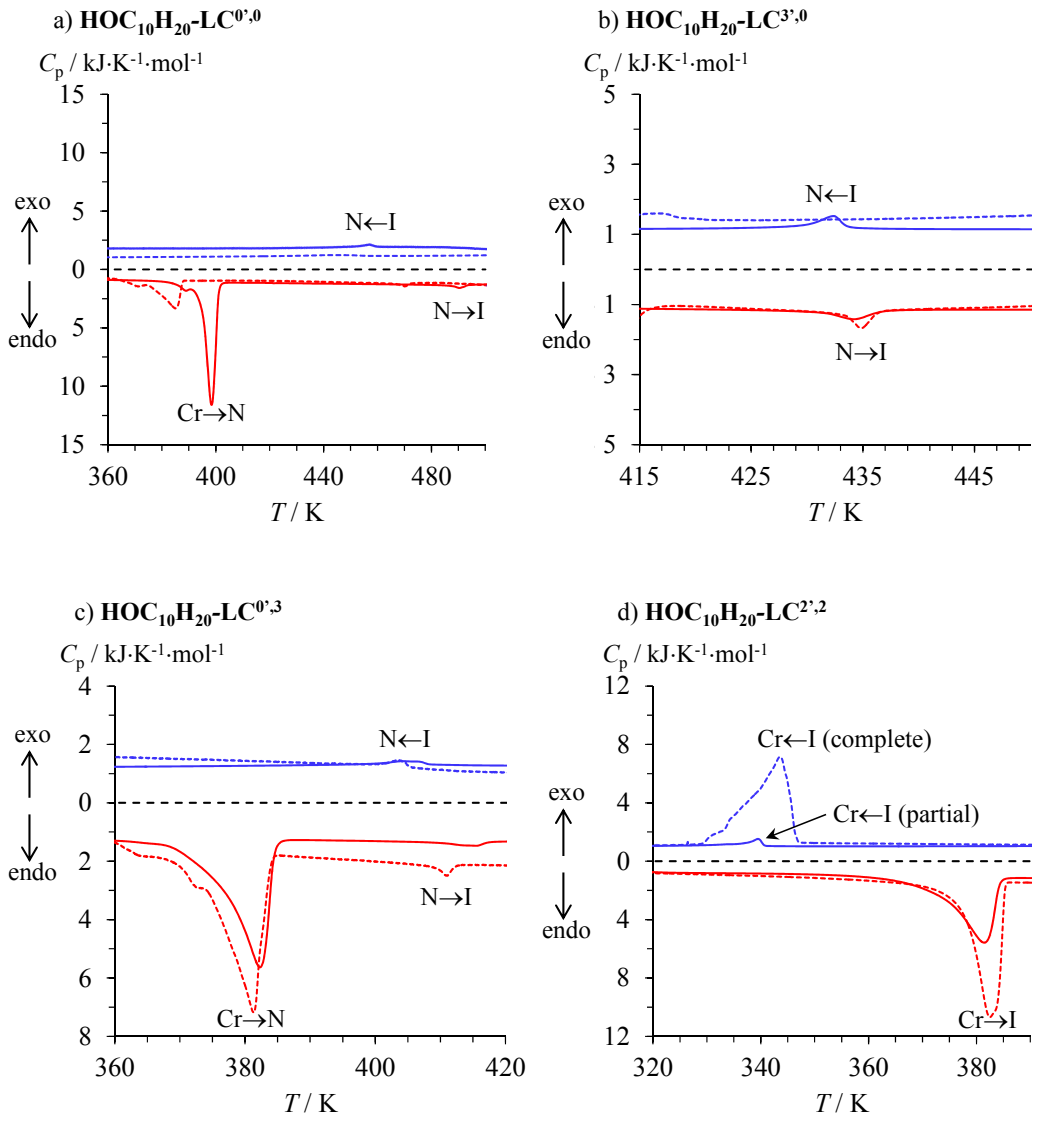

Figure S35 DSC thermographs of **HOC$_{10}$H$_{20}$-LC$^{i',j}$** (scan rates 10 K/min (full traces) and 0.5 K/min (dotted traces), heating cycle with downward peaks, cooling cycle with upward peaks). G = glass, Cr = crystal, SmA = smectic A, N = nematic, I = isotropic liquid.

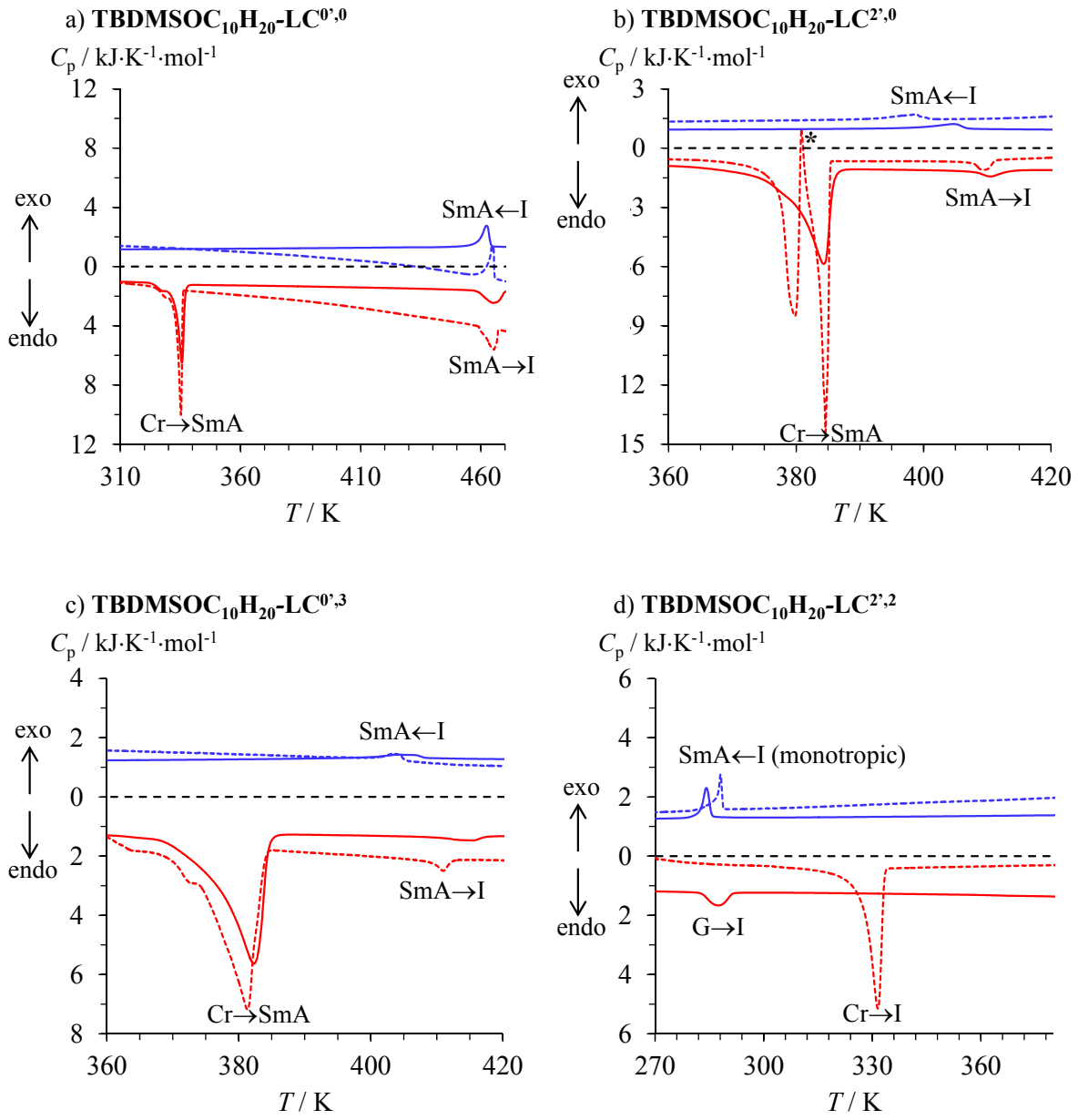

Figure S36 DSC thermographs of **TBDMSOC$_{10}$H$_{20}$-LC$^{i',j}$** (scan rates 10 K/min (full traces) and 0.5 K/min (dotted traces), heating cycle with downward peaks, cooling cycle with upward peaks). G = glass, Cr = crystal, SmA = smectic A, N = nematic, I = isotropic liquid and * = kinetically-delayed reorganization.

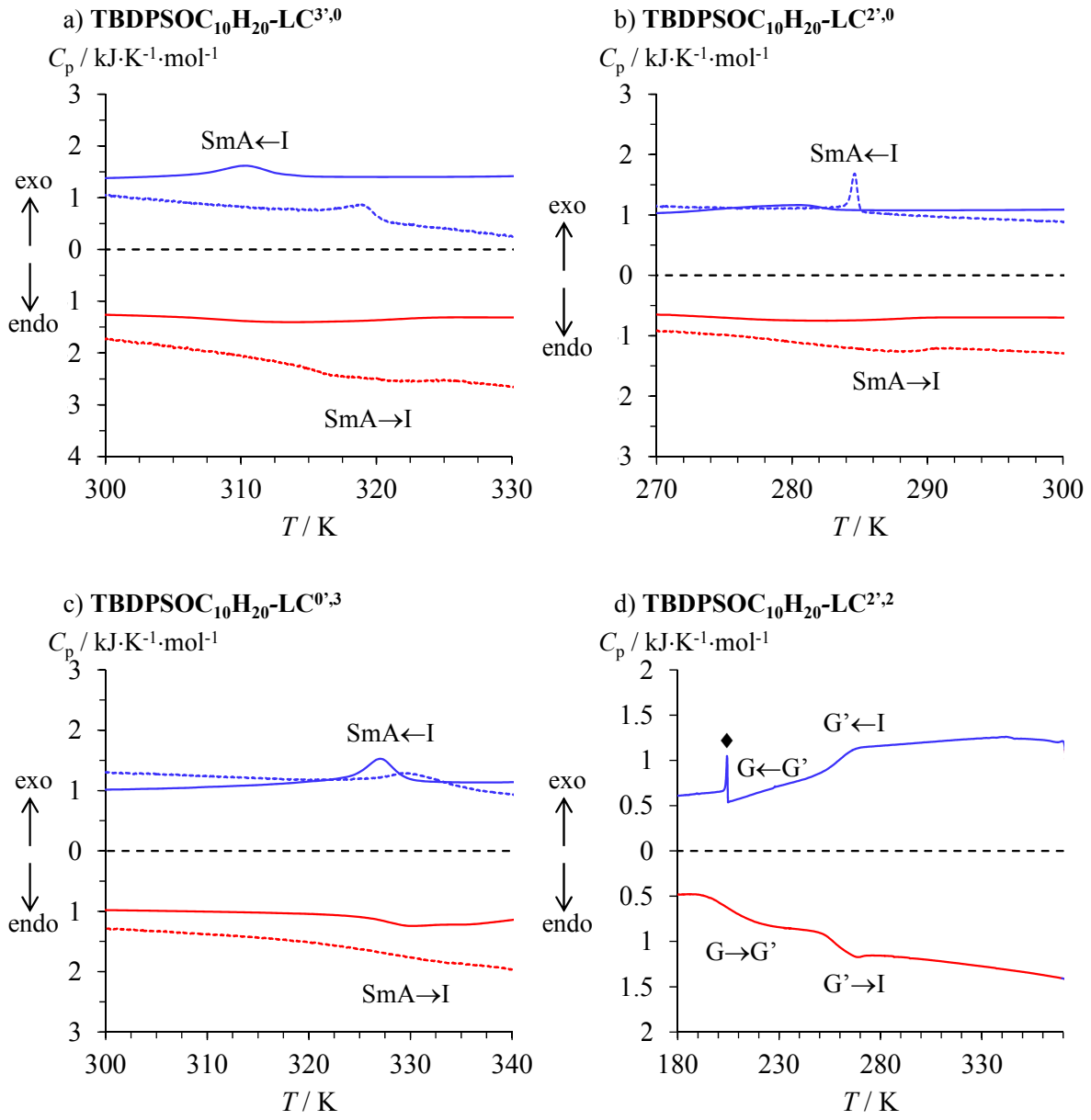

Figure S37 DSC thermographs of **TBDPSOC$_{10}$H$_{20}$-LC$^{i',j}$** (scan rates 10 K/min (full traces) and 0.5 K/min (dotted traces), heating cycle with downward peaks, cooling cycle with upward peaks). G = glass, Cr = crystal, SmA = smectic A, N = nematic, I = isotropic liquid. ♦ = low-temperature artefact of the heat-flow detector.

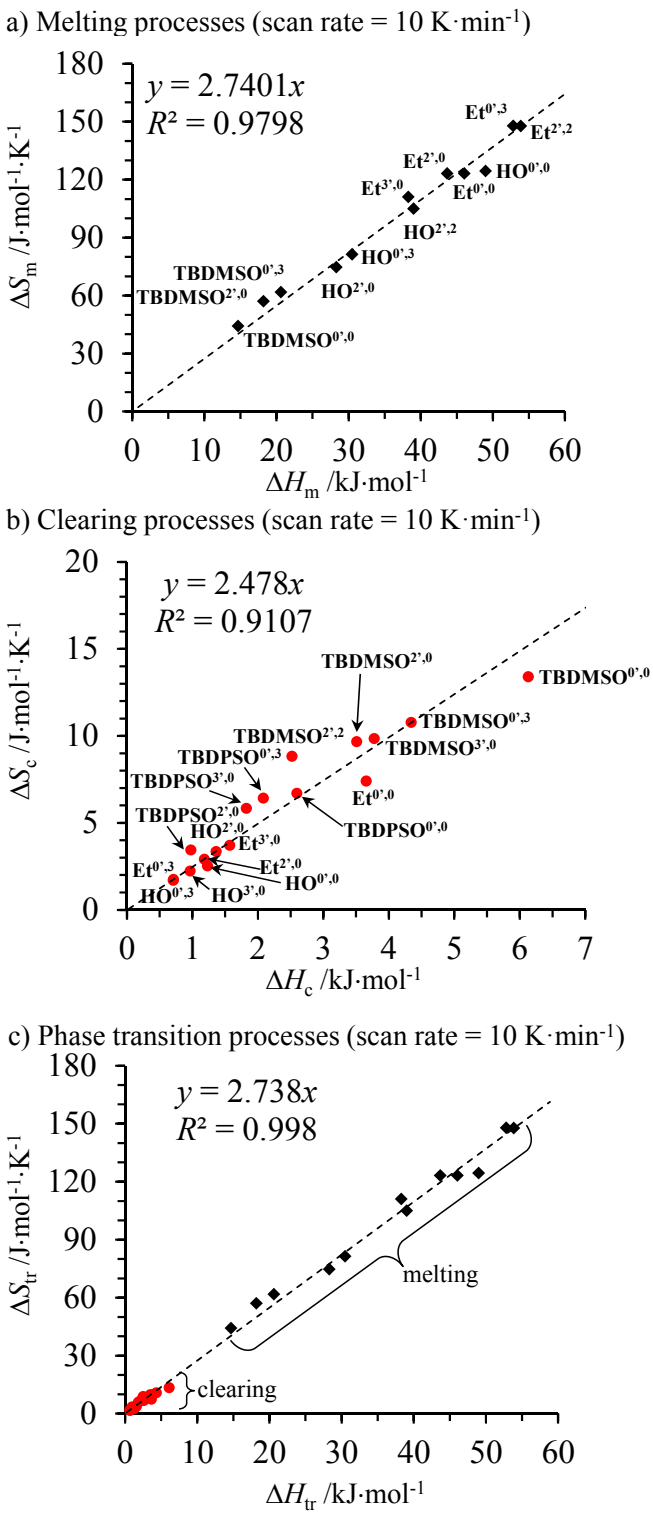

Figure S38 ΔS_{tr} *versus* ΔH_{tr} plots for a) the melting, b) the clearing and c) both phase transitions occurring in **R-C$_{10}$H$_{20}$-LC$^{i',j}$** (R = HO, Et, TDMSO, TPDPSO) showing linear *H*/*S* compensations (scan rates 10 K/min).

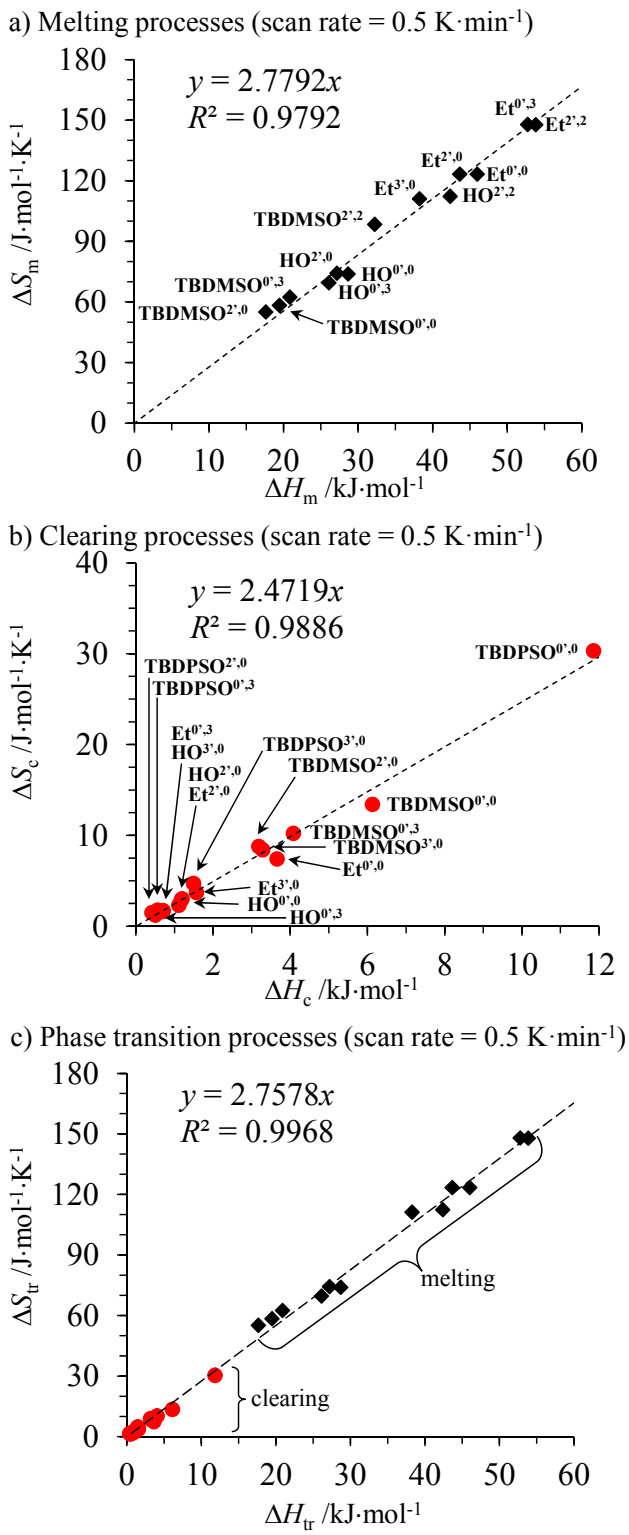

Figure S39 ΔS_{tr} *versus* ΔH_{tr} plots for a) the melting, b) the clearing and c) both phase transitions occurring in **R-C$_{10}$H$_{20}$-LC$^{i',j}$** (R = HO, Et, TDMSO, TPDPSO) showing linear *H*/*S* compensations (scan rates 0.5 K/min).

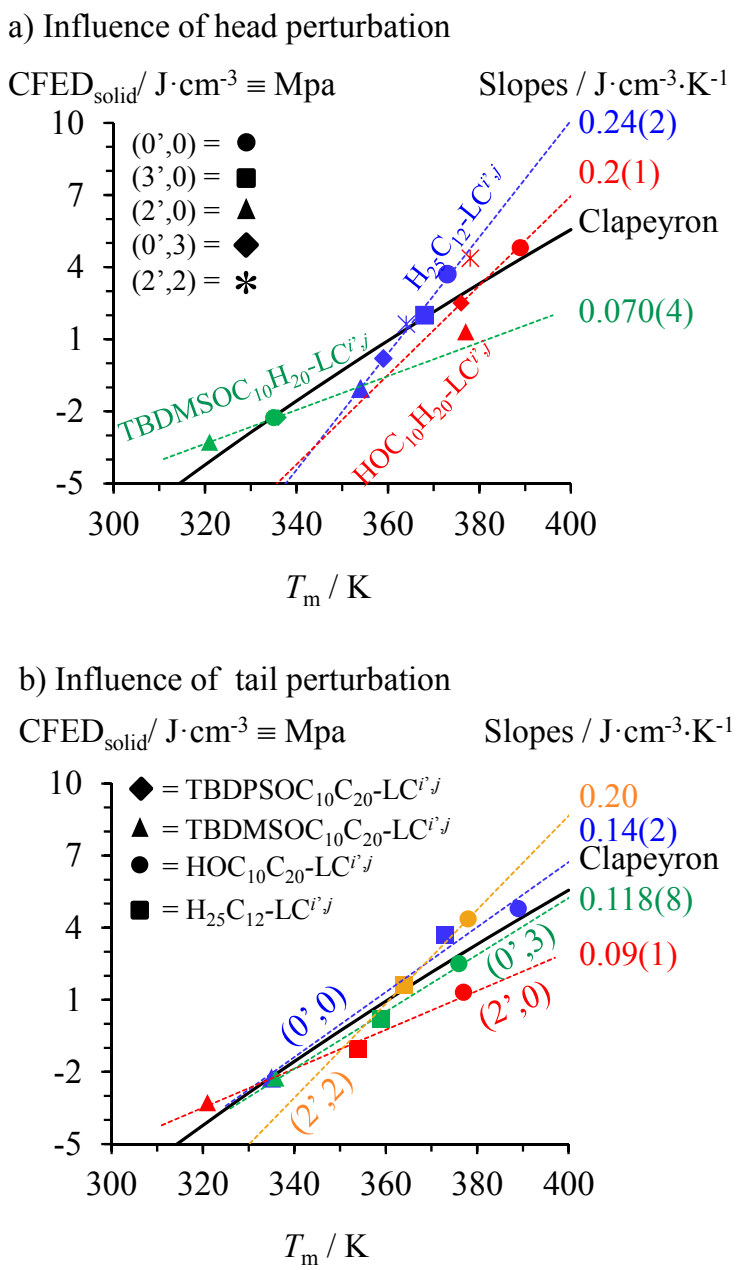

Figure S40 Cohesive free energy densities (CFED, scan rate = 0.5 K min^{-1}) versus transition temperatures for the melting processes highlighting a) the influence of head substitution and b) the influence of tail substitution. The full black traces correspond to the solid-liquid crystal boundary fitted with Clapeyron equation (eq. 7). The dotted colored traces show local linear correlations (eq. 8) for a) a given tail substitution and b) a given head substitution.

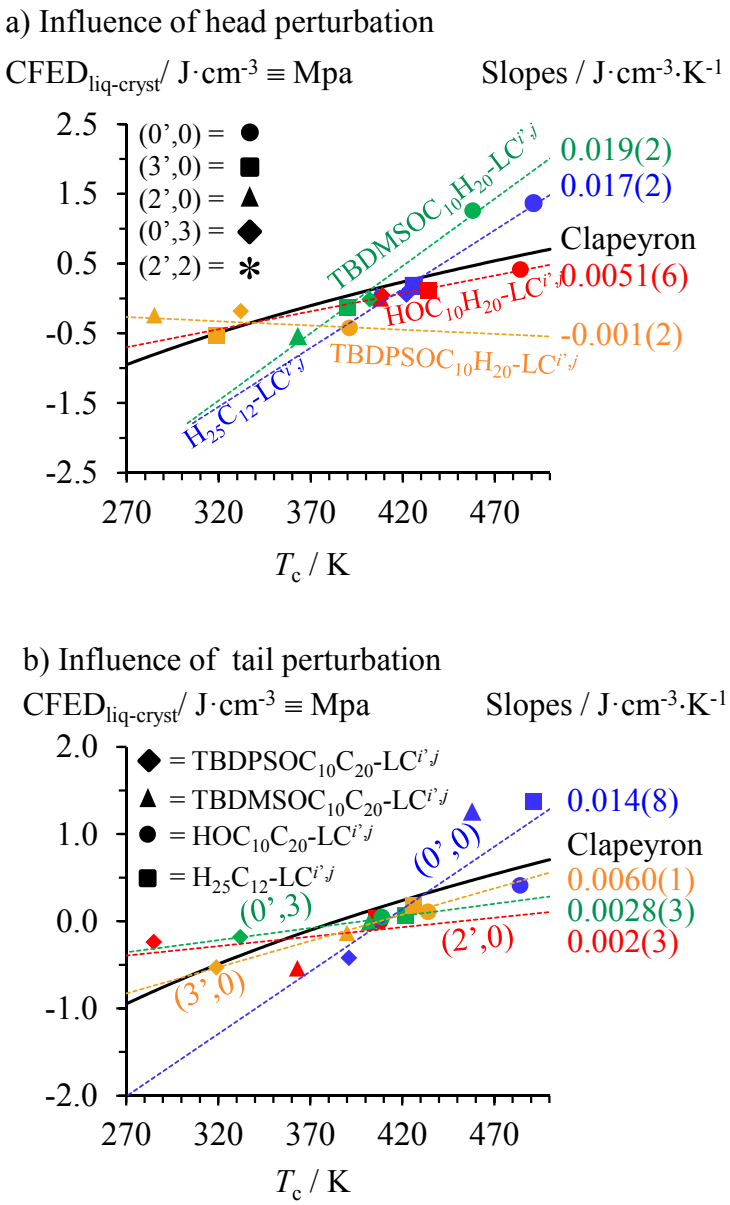

Figure S41 Cohesive free energy densities (CFED, scan rate = 0.5 K min^{-1}) versus transition temperatures for the clearing processes highlighting a) the influence of head substitution and b) the influence of tail substitution. The full black traces correspond to the liquid crystal-liquid boundary fitted with Clapeyron equation (eq. 7). The dotted colored traces show local linear correlations for a) a given tail substitution and b) a given head substitution.

Appendix 1 Molecular modeling and organization in the liquid crystalline phases for substituted cyanobiphenyls RO-$C_{10}H_{20}$-$LC^{i',j}$.

The molecular structures of the mesogens **TBDPSO-$C_{10}H_{20}$-$LC^{i',j}$**, **TBDMSO-$C_{10}H_{20}$-$LC^{i',j}$** and **HO-$C_{10}H_{20}$-$LC^{i',j}$** were optimized in the gas phase using the MM2 force field implemented in Avogadro program (Fig. A1-1 and Table A1-1).[A1-1] Whatever the size of the terminal moiety (H, TBDMS, TBDPS) attached to the terminal hydroxyl group, the flexible alkyl chains are roughly linear and adopt all trans configurations (Fig A1-1a). The polar aromatic cyanobiphenyl cores, made up of three successive phenyl rings, form a pseudo-linear rigid segment, in which the magnitude of the interplanar angles ϕ_1 and ϕ_2 vary (Fig. A1-1b). In line with the crystal structures of **$H_{25}C_{12}$-$LC^{i',j}$**,[A1-2] the interplanar angles between the two connected aromatic rings of the biphenyl are close to orthogonal (ϕ_1 = 85(3)°) for compounds having at least one methyl group bound to the 2 or 2' position, while relaxation to ϕ_1 = 55.4(7)° is characteristic for the less constrained biphenyls (Table A1-1). The roughly constant interplanar angle ϕ_2 = 78(7)° between the cyanobiphenyl unit and the benzoate substituent is not sensitive to the bound terminal groups (Fig. A1-1b). Finally, the two incompatible rod-like linear segments in the mesogenic compounds (*i.e.* flexible chain and rigid core) produce a slightly bent arrangement $\phi_{\text{head-tail}}$ = 153.5(6)°, which is reminiscent to that found in the crystal structures of **$H_{25}C_{12}$-$LC^{i',j}$** ($\phi_{\text{head-tail}}$ = 168(8)°, Fig. A1-1a).[A1-2]

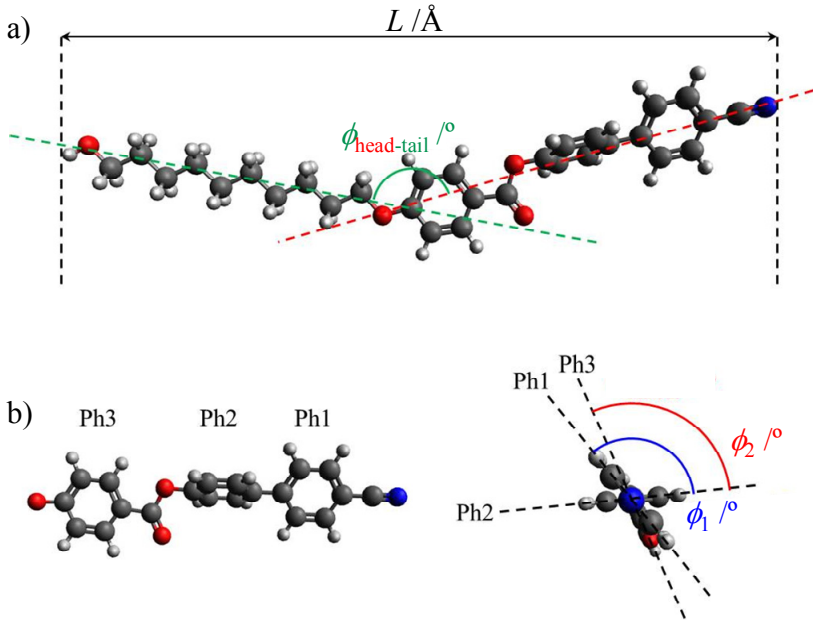

Figure A1-1 Gas-phase optimized molecular structure[A1-1] computed for H**O-$C_{10}H_{20}$-$LC^{0',0}$** and highlighting a) the bent arrangement ($\phi_{\text{head-tail}}$) of the aromatic (red dotted line) and

alkyl (green dotted line) linear segments, and b) the interplanar angles ϕ_1 and ϕ_2 characterizing the substituted cyanobiphenyl unit.

Table A1-1 Gas-phase optimized molecular structures computed for **HO-C$_{10}$H$_{20}$-LC$^{i',j}$**, **TBDMSO-C$_{10}$H$_{20}$-LC$^{i',j}$** and **TBDPSO-C$_{10}$H$_{20}$-LC$^{i',j}$** using the MM2 force field implemented in Avogadro program.[A1-1]

Compounds	L / Å	$\phi_{\text{head-tail}}$ / °	ϕ_1 / °	ϕ_2 / °	V_{molecule} / Å^3 [a]
HO-C$_{10}$H$_{20}$-LC$^{0',0}$	30.90	154.9	55.0	68.5	783.81
HO-C$_{10}$H$_{20}$-LC$^{3',0}$	30.92	153.0	55.9	72.1	812.32
HO-C$_{10}$H$_{20}$-LC$^{2',0}$	30.89	152.6	81.4	68.7	812.10
HO-C$_{10}$H$_{20}$-LC$^{0',3}$	30.92	152.7	56.7	69.5	811.50
HO-C$_{10}$H$_{20}$-LC$^{2',2}$	30.88	152.4	87.7	81.5	836.34
TBDMSO-C$_{10}$H$_{20}$-LC$^{0',0}$	35.22	152.9	54.8	73.2	979.76
TBDMSO-C$_{10}$H$_{20}$-LC$^{3',0}$	35.27	154.2	55.1	82.3	1009.85
TBDMSO-C$_{10}$H$_{20}$-LC$^{2',0}$	35.23	153.8	81.5	85.8	1009.04
TBDMSO-C$_{10}$H$_{20}$-LC$^{0',3}$	35.26	154.0	55.1	89.5	1009.27
TBDMSO-C$_{10}$H$_{20}$-LC$^{2',2}$	35.24	153.9	86.5	79.6	1033.95
TBDPSO-C$_{10}$H$_{20}$-LC$^{0',0}$	35.26	154.0	54.9	76.4	1161.52
TBDPSO-C$_{10}$H$_{20}$-LC$^{3',0}$	35.23	153.5	56.5	75.0	1184.86
TBDPSO-C$_{10}$H$_{20}$-LC$^{2',0}$	35.21	153.7	87.3	88.8	1182.45
TBDPSO-C$_{10}$H$_{20}$-LC$^{0',3}$	35.27	154.2	54.8	76.6	1183.65
TBDPSO-C$_{10}$H$_{20}$-LC$^{2',2}$	35.20	153.7	86.9	89.0	1207.65

[a] The molecular volumes are taken as the Connolly volumes.[A1-3]

The total length of the rod-like molecules increases from L = 30.90(2) Å for **HO-C$_{10}$H$_{20}$-LC$^{i',j}$** to L = 35.24(2)Å for **TBDMSO-C$_{10}$H$_{20}$-LC$^{i',j}$** and L = 35.23(3)Å for **TBDPSO-C$_{10}$H$_{20}$-LC$^{i',j}$** (Table A1-1). Compared with the periodicities d_{001} observed in the lamellar smectic A phases (Table A1-2), the $1.29 \leq d_{001}/L \leq 1.59$ ratios calculated for the silylated cyanobiphenyls suggest the formation of partially interdigitated bilayers (Fig. A1-2).[A1-4]

Table A1-2 Molecular length L (computed gas-phase geometry) and interlayer periodicites measured in the smectic A mesophases d_{001} for **TBDMSO-$C_{10}H_{20}$-LC$^{i',j}$** and **TBDPSO-$C_{10}H_{20}$-LC$^{i',j}$**

Compounds	L / Å	d_{001} / Å	d^{001}/L	Layering
TBDMSO-$C_{10}H_{20}$-LC$^{0',0}$	35.22	49.21	1.40	Interdigitated bilayer
TBDMSO-$C_{10}H_{20}$-LC$^{3',0}$	35.27	49.32	1.40	Interdigitated bilayer
TBDMSO-$C_{10}H_{20}$-LC$^{2',0}$	35.23	49.69	1.41	Interdigitated bilayer
TBDMSO-$C_{10}H_{20}$-LC$^{0',3}$	35.26	45.64	1.29	Interdigitated bilayer
TBDMSO-$C_{10}H_{20}$-LC$^{2',2}$	35.24	51.20	1.45	Interdigitated bilayer
TBDPSO-$C_{10}H_{20}$-LC$^{0',0}$	35.26	54.52	1.55	Interdigitated bilayer
TBDPSO-$C_{10}H_{20}$-LC$^{3',0}$	35.23	53.92	1.53	Interdigitated bilayer
TBDPSO-$C_{10}H_{20}$-LC$^{2',0}$	35.21	56.03	1.59	Interdigitated bilayer
TBDPSO-$C_{10}H_{20}$-LC$^{0',3}$	35.27	51.32	1.46	Interdigitated bilayer

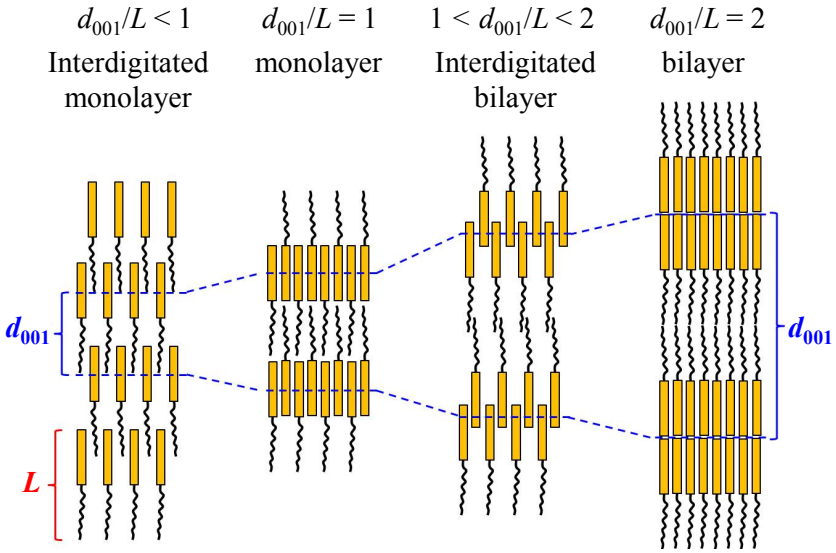

Figure A1-2 Schematic representation of the organization of the molecules in the smectic A mesophases with respect to increasing d_{001}/L ratios (see text). Code: orange rectangles = aromatic substituted cyanobiphenyl cores, black zig-zag traces = flexible alkyl chains.

A close scrutiny at Table A1-2 suggests that the weak, but significant increase of d_{001}/L in going from **TBDMSO-C$_{10}$H$_{20}$-LC$^{i',j}$** (average value = 1.39(6)) to **TBDPSO-C$_{10}$H$_{20}$-LC$^{i',j}$** (average value = 1.53(5)) can be tentatively assigned to intermolecular aromatic stacking interactions operating between bulky tert-butyldiphenyl silyl termini, which limit chain interdigitation (Fig. A1-3).

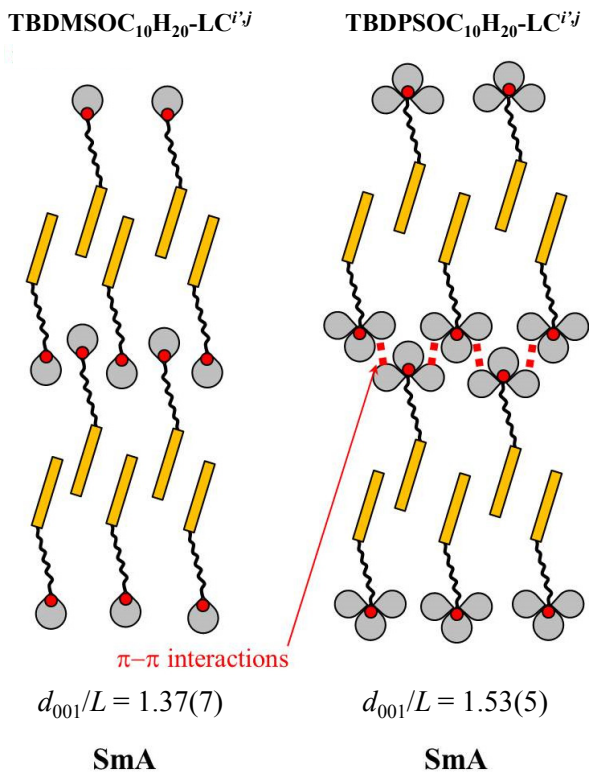

Figure A1-3 Schematic representation of the organization of the molecules in the smectic A mesophases with respect to average d_{001}/L ratios. Code: orange rectangles = aromatic substituted cyanobiphenyl cores, black zig-zag lines = flexible alkyl chains, grey lobes = silyl substituents.

Interestingly, the non-silylated compounds **HO-C$_{10}$H$_{20}$-LC$^{i',j}$** show only orientational order leading to the formation of nematic mesophases. In this context, we suspect that efficient intermolecular head-to-tail -CN···HO- hydrogen bonds operating in **HO-C$_{10}$H$_{20}$-LC$^{i',j}$** prevent lateral cohesions required for smectogenic behaviour (Fig. A1-4), but we were unable to grow X-ray quality monocrystals for substantiating this hypothesis.

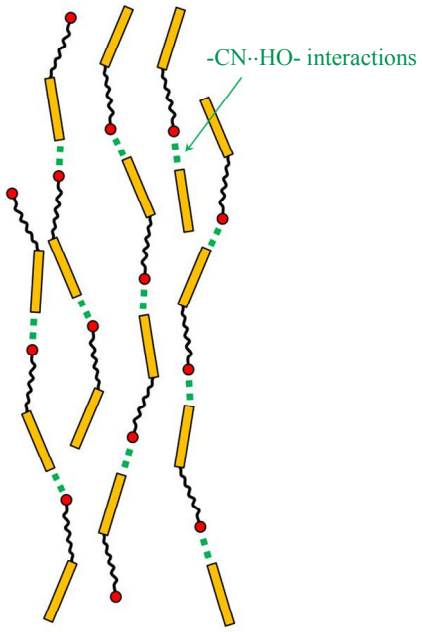

N

Figure A1-4 Schematic representation of the organization of the molecules in the nematic mesophases for **HO-$C_{10}H_{20}$-LC$^{i',j}$** Code: orange rectangles = aromatic substituted cyanobiphenyl cores, black zig-zag lines = flexible alkyl chains, red disks = hydroxyl groups.

References

A1-1 M. D. Hanwell, D. E. Curtis, D. C. Lonie, T. Vandermeersch, E. Zurek and G. R. Hutchison,. J. Cheminform., 2012, 4, 17. Avogadro 1.1.1 can be downloaded at http://avogadro.cc/wiki/Main_Page.

A1-2 T. Dutronc, E. Terazzi, L. Guénée, K.-L. Buchwalder, S. Floquet, C. Piguet, *Chem. Eur. J.*, 2016, **22**, 1385-1391.

A1-3 The molecular volumes are taken as the Connolly volumes, which are obtained from the building of the Connolly surface around the molecular structures of complexes observed in their crystal structure and by using a probe radius of 1.4 Å for modelling water solvent molecule (M. L. Connolly, *Science*, 1983, **221**, 709-713. M. L. Connolly, *J. Appl. Cryst.*, 1983, **16**, 548-558).

A1-4 W. Haase, Z. X. Fan and H. J. Muller, *J. Chem. Phys.*, 1988, **89**, 3317-3322

Appendix 2 Slow kinetic structural reorganizations operating in RO-$C_{10}H_{20}$-$LC^{i',j}$.

The DSC traces of the compounds **HO-$C_{10}H_{20}$-$LC^{2',0}$** (Fig. 5a), **TBDMSO-$C_{10}H_{20}$-$LC^{2',0}$** (Fig. S36b) and **TBDMSO-$C_{10}H_{20}$-$LC^{2',2}$** (Fig. S36d) displayed minor peaks, the enthalpies and onset temperatures of which vary with the scan rates. A detailed time-dependent investigation of the DSC traces and X-ray diffraction patterns suggested that these behaviours can be assigned to slow structural reorganizations operating in the glassy state after the first heating/cooling cycle. Taking **TBDMSO-$C_{10}H_{20}$-$LC^{2',2}$** as a model, one observed that, during the first hetaing-cooling cycle (, (Fig. A2-1), the crystalline phase melted to give an isotropic liquid at 59°C (332 K), which was transformed, upon cooling, into a monotropic smectic A mesophase at 16°C (289 K).

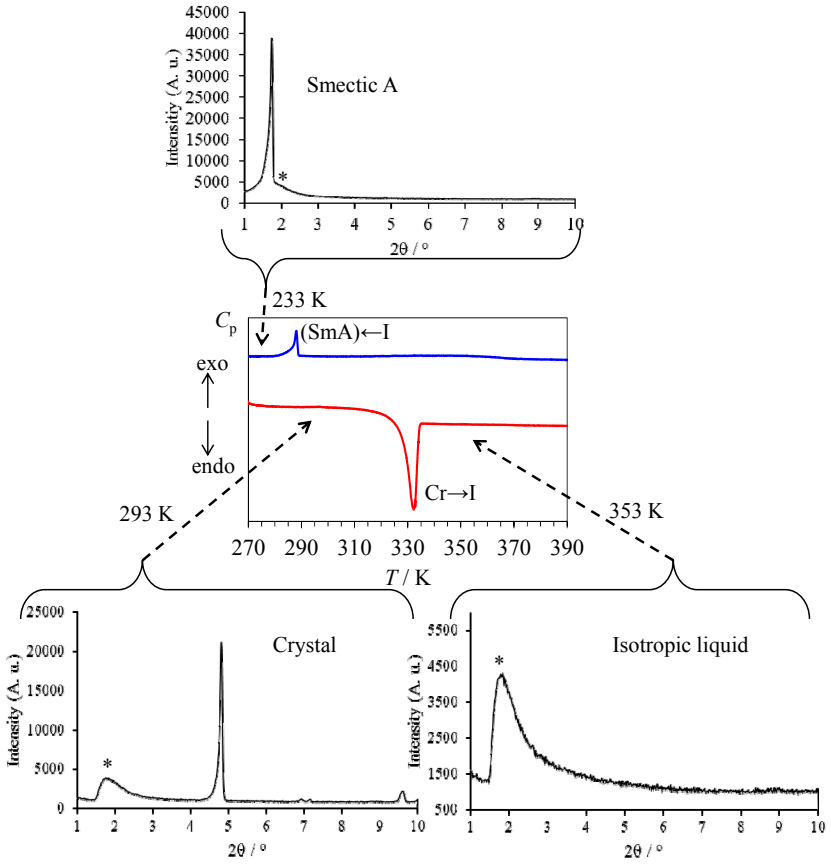

Figure A2-1 Thermograph of compound **TBDMSO-$C_{10}H_{20}$-$LC^{2',2}$** recorded at 0.5 K·min^{-1} during the first heating (red trace) and cooling (blue trace) cycle, and showing the X-ray diffraction patterns recorded at specified temperatures during the heating (bottom diffractograms) and cooling (top diffractogram) processes. * = capillary noise.

The record of a second heating/cooling cycle (Fig. A2-2) without delay showed two successive weak endothermic processes, while the introduction of a 24 hours delay restored the cristalline organization and the detection of a single Cr→I transition at 59°C (332 K, Fig. A2-3).

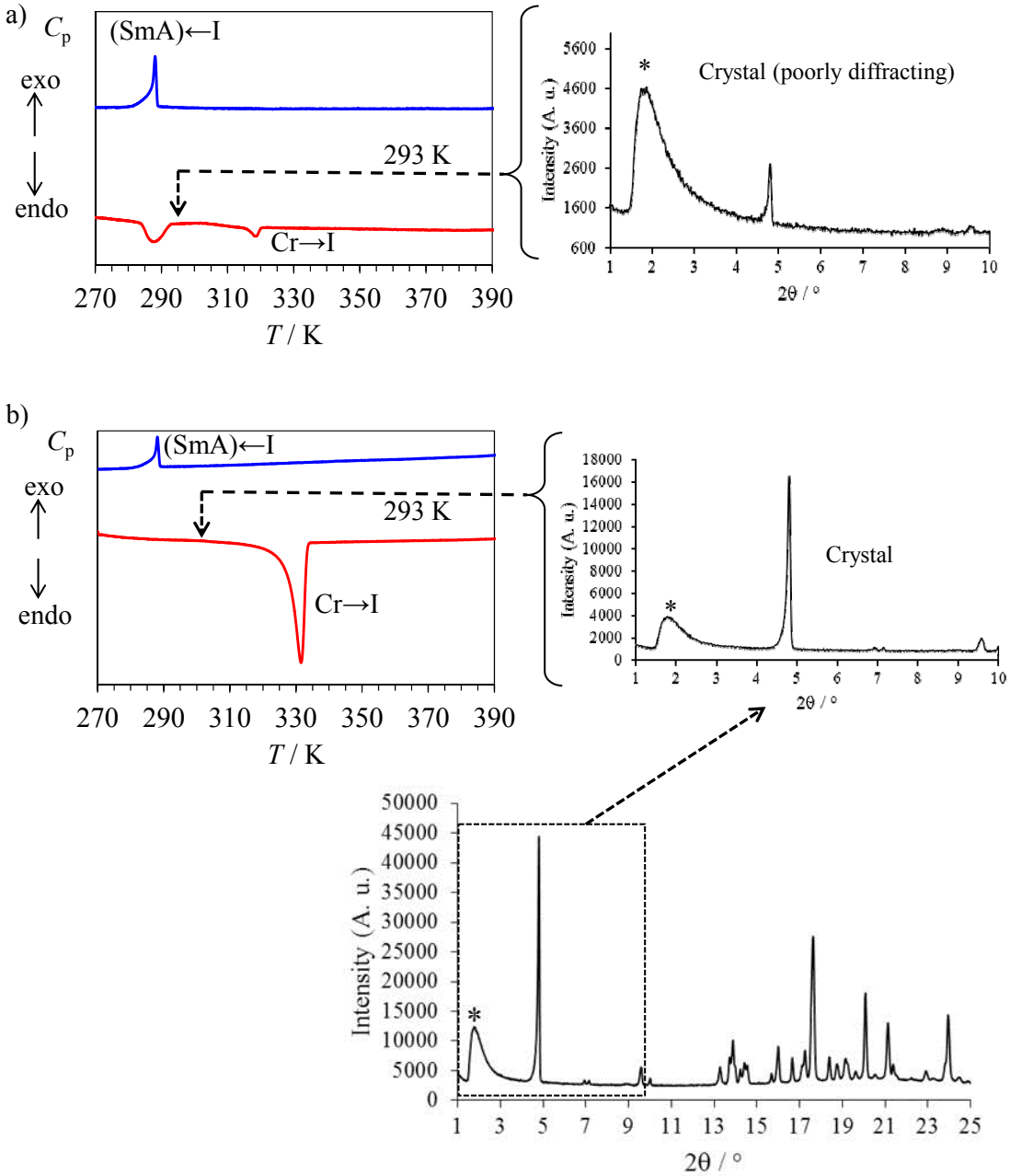

Figure A2-2 Thermographs of compound **TBDMSO-$C_{10}H_{20}$-LC$^{2',2}$** recorded at 0.5 K·min^{-1} during the second heating (red trace)-cooling (blue trace) cycle and showing the X-ray diffraction patterns recorded at 293 K during the heating processes. * = capillary noise. a) Recorded 2 hours after the first heating/cooling cycle. Recorded 26 hours after the first heating/cooling cycle.